Article

Current Biology

Muscular hydraulics drive larva-polyp morphogenesis

Graphical abstract

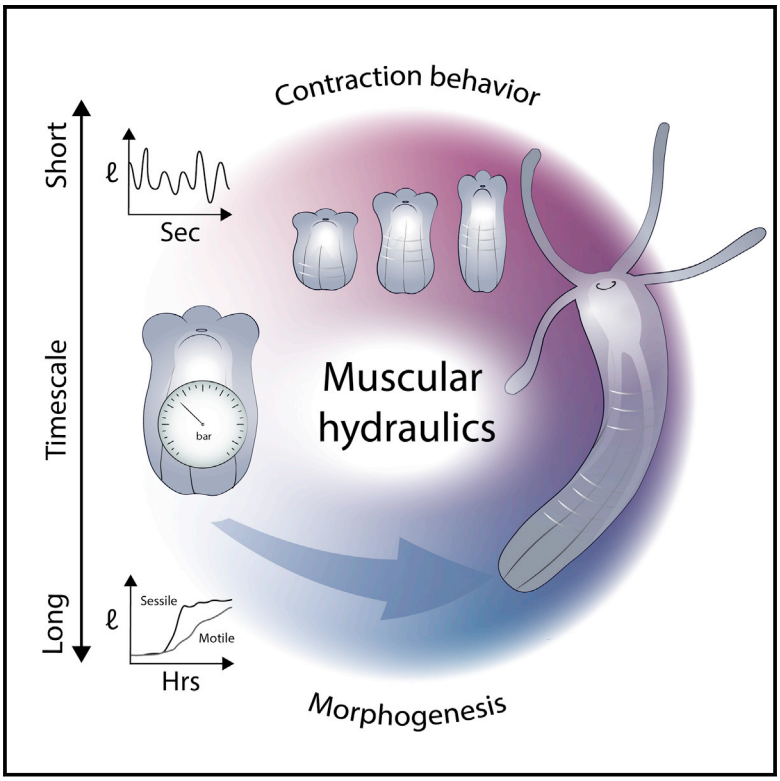

Authors

Anniek Stokkermans, Aditi Chakrabarti, Kaushikaram Subramanian, ..., Robert Prevedel, L. Mahadevan, Aissam Ikmi

Correspondence

lmahadev@g.harvard.edu (L.M.), aissam.ikmi@embl.de (A.I.)

In brief

Stokkermans et al. show that the muscular-hydraulic system that controls body movement drives size and shape changes in the cnidarian *Nematostella vectensis*. Furthermore, organismal contractility and motility impact the dynamics of morphological changes. These data link animal behaviors and morphogenesis at both cellular and biophysical levels.

Highlights

- Body contractility and motility influence the dynamics of larva-polyp morphogenesis
- The inflation of body cavity via hydraulics increases polyp size
- The organization of body wall muscles controls polyp shape
- Pressures generated by muscular hydraulics coordinate whole-body tissue remodeling

Stokkermans et al., 2022, Current Biology *32*, 1–12
November 7, 2022
https://doi.org/10.1016/j.cub.2022.08.065

CellPress

Please cite this article in press as: Stokkermans et al., Muscular hydraulics drive larva-polyp morphogenesis, Current Biology (2022), https://doi.org/10.1016/j.cub.2022.08.065

Current Biology

CellPress
OPEN ACCESS

Article

Muscular hydraulics drive larva-polyp morphogenesis

Anniek Stokkermans,[1,2] Aditi Chakrabarti,[3] Kaushikaram Subramanian,[1,4] Ling Wang,[1,4] Sifan Yin,[3] Prachiti Moghe,[1,2,5] Petrus Steenbergen,[1] Gregor Mönke,[1] Takashi Hiiragi,[1,5] Robert Prevedel,[1,4,6] L. Mahadevan,[3,7,*] and Aissam Ikmi[1,8,9,*]
[1]Developmental Biology Unit, European Molecular Biology Laboratory, 69117 Heidelberg, Germany
[2]Collaboration for Joint PhD Degree between EMBL and Heidelberg University, Faculty of Biosciences, 69117 Heidelberg, Germany
[3]School of Engineering and Applied Sciences, Harvard University, Cambridge, MA 02138, USA
[4]Cell Biology and Biophysics Unit, European Molecular Biology Laboratory, 69117 Heidelberg, Germany
[5]Hubrecht Institute-KNAW (Royal Netherlands Academy of Arts and Sciences), 3584 CT Utrecht, the Netherlands
[6]Epigenetics & Neurobiology Unit, European Molecular Biology Laboratory, 00015 Monterotondo, Italy
[7]Departments of Physics, and Organismic and Evolutionary Biology, Harvard University, Cambridge, MA 02138, USA
[8]Twitter: @AissamIkmi
[9]Lead contact
*Correspondence: lmahadev@g.harvard.edu (L. M.), aissam.ikmi@embl.de (A. I.)
https://doi.org/10.1016/j.cub.2022.08.065

SUMMARY

Development is a highly dynamic process in which organisms often experience changes in both form and behavior, which are typically coupled to each other. However, little is known about how organismal-scale behaviors such as body contractility and motility impact morphogenesis. Here, we use the cnidarian *Nematostella vectensis* as a developmental model to uncover a mechanistic link between organismal size, shape, and behavior. Using quantitative live imaging in a large population of developing animals, combined with molecular and biophysical experiments, we demonstrate that the muscular-hydraulic machinery that controls body movement also drives larva-polyp morphogenesis. We show that organismal size largely depends on cavity inflation through fluid uptake, whereas body shape is constrained by the organization of the muscular system. The generation of ethograms identifies different trajectories of size and shape development in sessile and motile animals, which display distinct patterns of body contractions. With a simple theoretical model, we conceptualize how pressures generated by muscular hydraulics can act as a global mechanical regulator that coordinates tissue remodeling. Altogether, our findings illustrate how organismal contractility and motility behaviors can influence morphogenesis.

INTRODUCTION

During development, animals not only undergo morphological changes but also acquire a complex repertoire of organismal-scale behaviors such as contractility and motility. Although these behaviors drive body movement and are crucial for animal survival in their natural habitats, the physical forces underlying these processes can also generate mechanical stresses on developing tissues.[1,2] Force generation through actomyosin-mediated contractility is a highly conserved mechanism that drives muscle contraction, cell deformation, and tissue morphogenesis.[3] However, understanding how large-scale active deformations in a freely developing organism impact morphogenesis remains a challenge.[4] Most leading morphogenesis studies provide in-depth, high spatial resolution views of early development, yielding insights into how embryonic mechanisms drive development at the single-cell resolution and a wide range of timescales.[5–9] By contrast, behavioral studies commonly track whole-body actions in the environment over finer timescales.[10,11] These differences preclude understanding how whole-organism coordination of morphogenesis is achieved in a freely developing animal and reflect limitations of technologies and model systems used in development and behavior research. Therefore, studying the potential relationship between morphogenesis and intrinsic organismal behaviors requires a system in which both processes can be studied simultaneously, ideally with minimal environmental complexity.

Cnidarians have a relatively simple diploblastic architecture composed of two epithelial layers surrounding a single fluid-filled cavity with an oral opening and are organized along a polarized oral-aboral body axis.[12–15] Larva-polyp morphogenesis is a key morphogenetic process that transforms a free-swimming stage into a sedentary form with oral tentacles.[15,16] In some cnidarians, including coral and hydrozoan species, transforming larvae undergo a cue-driven metamorphosis that involves drastic tissue remodeling with extensive cell proliferation and apoptosis.[17–20] By contrast, in the sea anemone *Nematostella vectensis*, this transformation is a smooth transition that progressively elongates the initial ovoid morphology into a tubular polyp and

Please cite this article in press as: Stokkermans et al., Muscular hydraulics drive larva-polyp morphogenesis, Current Biology (2022), https://doi.org/10.1016/j.cub.2022.08.065

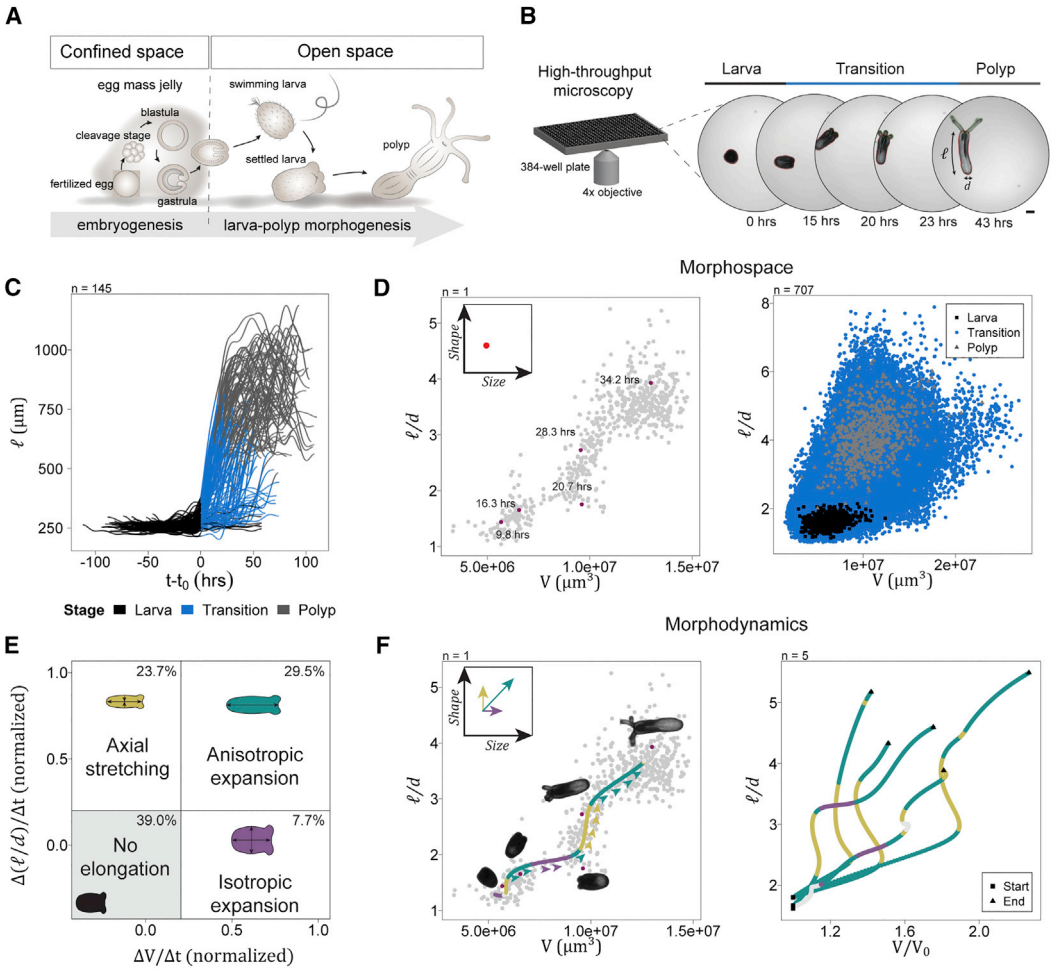

Figure 1. High-throughput live imaging of larva-polyp transition

(A) Schematic of *Nematostella* development.

(B) Experimental setup.

(C) Smoothed curves for body column length (ℓ), shifted in time by t_0, which marks the start of larva-polyp transition (n = 145 animals from a single experiment).

(D) Left: measurements in morphospace for a single animal. Right: morphospace plot for indicated developmental stages (n = 707 animals).

(E) Morphodynamics based on normalized changes in body column volume and aspect ratio (n = 707 animals).

(F) Left: measurements in morphospace with overlaid morphodynamics, indicated by color (purple: isotropic expansion; yellow: axial stretching; green: anisotropic expansion; and gray: no elongation). Right: smoothed larva-polyp transition trajectories in relative size-shape morphospace for five animals.

Scale bars, 100 µm.

See also Figure S1 and Video S1.

does not appear to require any environmental stimuli.[21,22] Despite these differences among cnidarian species, they all exhibit discrete behaviors such as swimming, settlement, and body contractions,[16,23] offering a developmental context to map connections between dynamic behavioral modes and morphogenetic processes. However, a significant bottleneck in the field is the lack of live imaging strategies that capture the dynamics of this life-history transition. Given the gradual morphological transformation, genetic tractability and optical accessibility of *Nematostella vectensis*,[12,24–26] we used this sea anemone as a developmental system to examine the mechanical drivers of larva-polyp morphogenesis and how this dynamic process copes with organismal behaviors in an open aquatic environment (Figure 1A).

RESULTS

Larva-polyp morphogenesis shows variability in morphodynamics

We established a high-throughput live imaging method that monitors larva-polyp morphogenesis in a controlled microenvironment for ~7 days at 5-min time resolution (Video S1; Figure 1B, n = 707 animals). Due to the asynchronous development between individuals, we used changes in circularity (a perfect circle is 1) of the whole-organism shape contours as a geometrical feature to classify the developmental stages into larva (circularity >0.8), larva-polyp transition (circularity of 0.3–0.8), or polyp (circularity <0.3) (Figures S1A and S1B). We found that animal circularity decreases dramatically during larva-polyp transition, which is

attributed to a 3- to 4-fold change in the length of the body and the development of oral tentacles (Figures 1C, S1A, and S1B). The population scale dynamics of larva-polyp transition were highly variable, and the overall time for development ranged from 16 to 30 h in most cases (Figures 1C and S1C). This variability was independent of the disparity in body lengths (Figure S1D).

To quantify morphological changes, we used the estimated body column volume and length/diameter body aspect ratio as features to monitor the changes in organismal size and shape, respectively (see STAR Methods). Mapping these two features together reveals a morphospace that animals explore during larva-polyp morphogenesis (Figure 1D). Although larvae generally have a smaller body column volume and aspect ratio compared with primary polyps, transitioning animals explore a wide range of combinations of different volumes and aspect ratios (Figure 1D). To investigate whether animals change their size and shape simultaneously or separately, we defined four categories of morphodynamics that reflect different phases during larva-polyp transition: (1) a change in size without a major aspect ratio increase, termed "isotropic expansion" (IE), (2) an increase in aspect ratio without major volume increase, termed "axial stretching" (AS), (3) a combined increase of both body column volume and aspect ratio, termed "anisotropic expansion" (AE), and (4) no substantial positive change in neither volume nor aspect ratio, termed "no elongation" (NE) (Figures 1E and 1F). Mapping morphodynamics over time shows that all four categories are deployed but that AE and AS are most frequently deployed during elongation (Figure 1E). However, the sequence and duration of different morphodynamics varied across developing animals (Figure 1F). Together, these data suggest that larva-polyp morphogenesis is guided by a relatively plastic developmental program.

Coordination of larva-polyp morphogenesis with behavioral modes

Marine invertebrate larvae typically undergo settlement that marks a shift from a free-swimming to a sessile form that can adhere to a substrate.[27,28] To study this behavioral change and link it to developmental dynamics, we tracked motility by measuring body displacement during all time points of the transition stage (n = 707 animals). We defined a low motility state when displacement is $\leq$130 μm per 5-min time interval and a high motility state if displacement is >130 μm (Figure S1E). Interestingly, the rate of body elongation was significantly higher in the low motility state compared with the high motility state (Figures S1F and S1G). To investigate motility behavior at the level of individual animals, we mapped their displacement during the transition stage and classified each animal as sessile (n = 517 out of 707; median displacement $\leq$130 μm) or motile (n = 190 out of 707; median displacement >130 μm). In addition to differences in the elongation rate (Figures 2A and 2B; Video S1), sessile and motile animals were markedly different in their morphospace and morphodynamics (Figures 2C–2E). Sessile animals showed a developmental period dominated by initial AE followed by AS (Figure 2D). This sequential pattern was absent in motile animals (Figure 2D). As a result, sessile animals typically had a higher aspect ratio at the same body column volume compared with motile animals, which led to noticeable differences in polyp shape (Figure 2C).

We next imaged animals at 5 seconds time resolution to distinguish between body deformations stemming from contractility behaviors versus morphogenesis (Figure S1H). On short timescales (seconds to minutes), reversible body deformation can be observed, resulting from contractility behavior, whereas irreversible changes underlying the morphogenetic transition take place over long timescales (hours). We generated kymographs to visualize body contractions along the oral-aboral axis (Figures 2F and S1I) and link patterns of body contractility with morphodynamics. We observed three qualitatively different contractions: (1) longitudinal contractions along the body length, (2) circumferential contractions that lead to peristaltic waves, and (3) a third type that corresponds to squeezing deformations that involve simultaneous local and/or global circumferential deformations. In sessile animals, early peristaltic waves co-occurred with both AE and IE (Figure 2F; Video S1), whereas the following AS phase typically involved "squeezing" behaviors (Figure 2F; Video S1). The low motility state in sessile animals often coincided with the onset of AS (Figures 2D and 2F), combined with aboral pole attachment (Figure S1G). As development progresses, peristaltic waves appear to become more frequent and coincide with further AS and/or AE of the body column (Figure 2F; Video S1, n = 25 sessile animals). In motile animals, squeezing and peristaltic waves were subtle and seemingly interrupted by longitudinal contractions that contribute to animal displacement (Figure S2A; Video S1, n = 2 motile animals), which most likely disrupted the dynamics of body elongation. Altogether, these ethograms show a robust correlation of morphodynamics with behavioral modes.

Larva-polyp morphogenesis requires muscular hydraulics

Cnidarian polyps are characterized by a muscular body wall surrounding a fluid-filled cavity, forming a hydrostatic skeleton. This muscular-hydraulic system uses internal fluid to transmit muscular forces required for body support and movement.[29–31] Typically, muscle contractions modulate cavity pressure and lead to reversible body deformations at short timescales.[29–31] To test the effect of muscle contraction on cavity pressure, we used a micropressure probe[32,33] to directly measure the luminal pressure in primary polyps. The static luminal pressure was approximately 1,000 Pa, which increased to about 6,000 Pa during the peristaltic wave (Figure 3A; Video S2). When animals were treated with the anesthetic $MgCl_2$, this dynamic pressure increase was abolished (Figure 3A; Video S2). Some primary polyps showed a static luminal pressure close to a null value (Video S2), which most likely reflects an open mouth state of the polyp. In this case, the peristaltic wave did not impact the pressure. This suggests that intrinsic behavioral patterns during the larva-polyp transition may result in a series of hydraulically driven body deformations that gradually lead to long-term morphogenetic change. Larvae already possess a primordial hydrostatic skeleton that further expands its luminal cavity during development (Figure S2B). To measure the relative contributions of tissue and luminal volume increase to body size, we acquired 3D morphological data in live larvae and their corresponding polyps using a custom-made dual-view optical coherence microscope (Figure S2C). The strong, label-free contrast between the tissue and the water-filled cavity permitted quantitative 3D

Please cite this article in press as: Stokkermans et al., Muscular hydraulics drive larva-polyp morphogenesis, Current Biology (2022), https://doi.org/10.1016/j.cub.2022.08.065

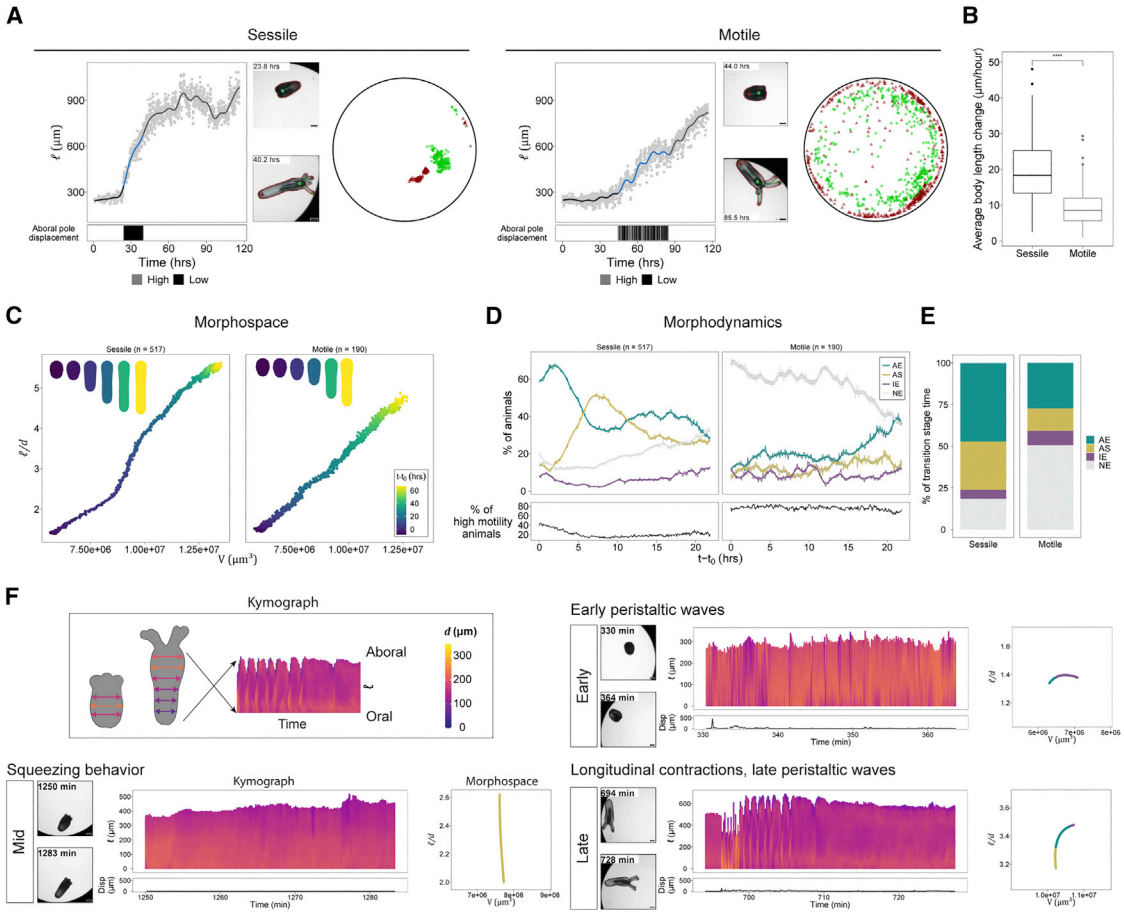

Figure 2. The dynamics of larva-polyp transition depend on behavioral modes

(A) Axial elongation dynamics for a sessile and motile animal. The positions of the oral (green dot) and aboral (red triangle) poles are shown for each behavior.

(B) Average axial elongation rate in sessile and motile animals (two-sided unpaired Wilcoxon test; ****$p < 0.0001$).

(C) Morphospace plot showing the averaged trajectory of sessile and motile animals in pseudotime. Insets show the averaged reconstructed body column shapes.

(D) Time-shifted distribution of morphodynamics for sessile and motile animals. AE, anisotropic expansion; AS, axial stretching; IE, isotropic expansion; NE, no elongation.

(E) Bar plot showing the percentage of transition stage time spent in the different categories of morphodynamics (n = 517 sessile and n = 190 motile animals).

(F) Ethograms showing examples of contractile and motile behaviors. Left: images of the beginning and end points for plotted time segments. Middle: kymographs showing body column diameter (color gradient) along the oral-aboral axis and animal displacement plots over time. Right: corresponding morphodynamics.

Scale bars, 100 µm.

See also Figures S1 and S2 and Video S1.

imaging at a high and near-isotropic spatial resolution, even in more light scattering larval stages, due to the dual-view geometry (see STAR Methods). The body cavity volume increased approximately 9-fold, whereas total tissue volume changed only around 1.5-fold (Figures 3B and S2D). Therefore, fluid uptake through inflation of the body cavity is a major contributor to final polyp size.

To examine the role of muscular hydraulics during development, we first tested different anesthetics on body contractility in primary polyps.[34,35] Although all anesthetics dramatically reduced body contractions (Figure S2E; Video S3), treatment with linalool resulted in a shape change in which the body column reverted to a wider and shorter morphology while the total volume of the animal remained largely unaffected (Figure S2F; Video S3). This suggests that the shape maintenance of primary polyps requires the basal tonus of the body wall to keep the tubular morphology. However, unlike linalool, $MgCl_2$-treated polyps largely maintained their overall shape but decreased in volume (Video S3), suggesting that different anesthetics distinctly affect the properties of the body wall and cavity. Nevertheless, exposing larvae to these anesthetics blocked body elongation and cavity inflation (Figure S2G). To directly link larva-polyp morphogenesis to hydraulic stresses, we inserted an either perforated or non-perforated hollow glass capillary through the mouth and the body column (Figure 3C). Although this does not disrupt body contractions (Video S4), perforated capillaries facilitate water exchange between the cavity and the external environment and thereby prevent the buildup of pressure inside the cavity. Control animals pierced with a non-perforated

Please cite this article in press as: Stokkermans et al., Muscular hydraulics drive larva-polyp morphogenesis, Current Biology (2022), https://doi.org/10.1016/j.cub.2022.08.065

CellPress
OPEN ACCESS

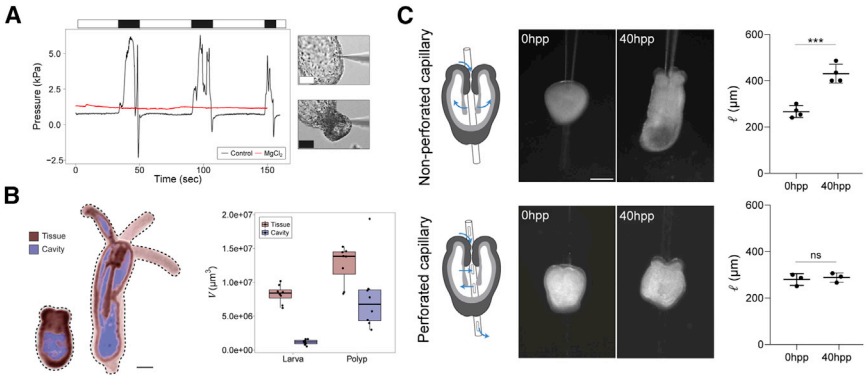

Figure 3. Muscular hydraulics is required for larva-polyp morphogenesis

(A) Cavity pressure in a contracting and a $MgCl_2$-treated animal.

(B) Left: mid-plane sections of 3D views of OCM images of the same animal at larva and polyp stage, segmented into tissue (red) and cavity (blue). Right: the quantification of tissue and cavity volume at larva and polyp stage (n = 8 animals).

(C) Mechanical perturbation of cavity pressure by insertion of a non-perforated capillary (control) or a perforated capillary (two-tailed unpaired t test, ***$p < 0.001$; ns $p > 0.05$). hpp, hours post perforation. The data are means ± SD. For non-perforated capillary, n = 4 biologically independent replicates. For perforated capillary, n = 3 biologically independent replicates.

Scale bars, 100 µm.

See also Figure S2 and Videos S1, S2, S3, and S4.

capillary successfully underwent larva-polyp transformation. By contrast, larvae punctured with a perforated capillary failed to elongate, arresting their development at the budded stage, thus mimicking the developmental phenotype caused by anesthetics (Figures 3C and S2G). Together, these findings indicate that a functional muscular-hydraulic system with a closed, pressurized cavity is essential for larva-polyp morphogenesis.

A physical model of larva-polyp morphogenesis

To connect larva-polyp morphogenesis to the dynamics of muscular hydraulics, we introduce a minimal biophysical framework that treats the larva as a soft cylindrical shell capable of ingesting fluid to increase cavity volume (Figure 4A). Consistent with observations of tissue organization and musculature, we assume that the body wall is anisotropic and much stiffer circumferentially than axially (see STAR Methods). Furthermore, for the passive rheology of the body wall, we assume a Zener-Kelvin-Voigt-like constitutive relation, with an elastic-plastic element (Young's modulus E^p and yield stress σ^y) attached in parallel to a viscous dashpot (viscosity η). Body wall activity is modeled using a muscular spring (E^a) attached in series with the passive elements as well as an active contractile element (σ^A) attached in parallel (Figure 4A). This configuration leads to an elastic response at short timescales and slow creep at long timescales that can be driven by a combination of intrinsic activity (e.g., muscular forces) and external loading (e.g., via the boundaries and hydraulic pressure). The assumed rheology is consistent with the published literature[36] and our own observations that the shape relaxation of the polyps upon exposure to linalool is viscoelastic in nature (Video S3).

For a thin cylindrical shell with length $\ell(t)$, radius $r(t)$, wall thickness $h(t)$, the axial and azimuthal stresses are described by: $\sigma_z = Pr/(2h)$ and $\sigma_\theta = Pr/h$, where $P(t)$is the intra-luminal pressure. At the simplest level, we can write this pressure as $P(t) = p_T + p_0 \cos(2\pi\omega t)$ where p_T is the base (static) pressure and p_0 is the amplitude of the oscillatory (dynamic) pressure term with ω being the contractile frequency. We refer to the static pressure as the priming component due to the steady active muscle tone that pressurizes the body cavity and to the oscillatory component as the pumping term that leads to a dynamic increase of pressure in the body cavity driven by muscular contractility. In Figure 4B, we show how cycles of priming and pumping lead to loading and unloading associated with the oscillations of pressure. The static (priming) pressure brings the axial wall stress close to the yield stress σ^y and the dynamic (pumping) oscillatory pressure term causes the wall to yield irreversibly. If the yield stress satisfies the inequality $p_T < 2\sigma^y h/r_0 < p_T + p_0$, the body wall follows an oscillatory elongation profile consistent with the correlation between axial length increase and body contractility (Figures 2F and S1I), via cycles of irreversible yielding and elastic recovery (Figure 4B). This then leads to a reduction of the polyp radius and an increase in its length, until eventually, the stress does not rise up to the level of yielding, leading to a remodeled body wall that reversibly contracts and expands due to periodic muscular contraction (see STAR Methods). A qualitative view of the larva-polyp transformation follows from the dynamic trajectories of body length $\ell(t)/\ell_0$ and radius $r(t)/r_0$ as a function of time as shown in Figure 4C and Video S5. Collectively, these results show that a combination of static and dynamic luminal pressure can cause the body wall to yield irreversibly, linking behavioral dynamics and larva-polyp morphogenesis.

Disruption of muscle organization affects size and shape

A key assumption of the model is that stiffness anisotropy of the body wall determines the direction of tissue expansion. Since the most natural potential source of anisotropy stems from muscle fiber orientation, we investigated the role of muscle organization in larva-polyp morphogenesis. The muscle system of the body wall consists of azimuthally oriented circular muscles (CMs) and axially oriented longitudinal parietal and retractor muscles (RMs)[37] (Figure 5A). The quantitative analysis of endodermal actin-rich filaments showed that muscle differentiation was visible at mid-larval stages. The circular and longitudinal orientations were progressively established over time, forming a well-organized muscular system prior to body elongation (Figures 5B and S3A). To reduce the complexity of the muscular system, we took advantage of the *BMP2/4* knockdown (KD) animals that maintain CM organization while lacking the secondary body axis, including the mesenteries and their associated longitudinal muscles (parietal and retractor).[38,39] Despite this dramatic change in body plan

Please cite this article in press as: Stokkermans et al., Muscular hydraulics drive larva-polyp morphogenesis, Current Biology (2022), https://doi.org/10.1016/j.cub.2022.08.065

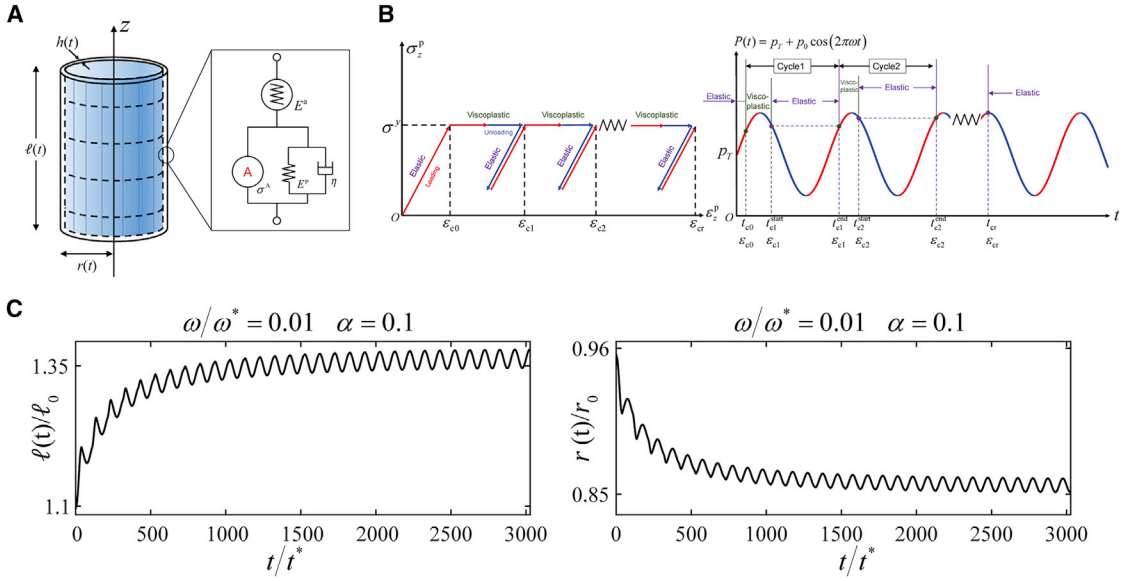

Figure 4. A biomechanical model of larva-polyp morphogenesis

(A) *Nematostella* modeled as a cylindrical shell.

(B) Left: loading-unloading cycle depicted in stress-strain space (see STAR Methods). Right: as the pressure oscillates about the mean tonus, the shell responds elastically before it yields and flows irreversibly until the pressure-induced stress falls below the yield point. The same process repeats itself in every cycle.

(C) Length and radius of the shell as a function of time with loading frequency $\omega/\omega^* = 0.01$ and yielding parameter $\alpha = 0.1$ obtained by solving (Equations 1, 2, 3, 4 and 5) (see STAR Methods for further details).

See also Video S5.

organization and morphodynamics (Figures 5C–5E; Video S6), the settlement behavior was largely unaffected, as we identified both populations of sessile and motile animals in the *BMP2/4* KD condition (Figures 5F and 5G). However, the repertoire of body contractions in *BMP2/4* KD was mainly reduced to the squeezing behavior (Figure S4A; Video S7), which resulted in AS the dominant driver of the elongated noodle-like shape (Figures 5D and 5H; Video S7). The rapid expulsion of fluid through the oral pole suggests that *BMP2/4* KD animals can pressurize their cavity (Figure S3C; Video S6). In addition, the treatment of *BMP2/4* KD larvae with anesthetics blocked this extreme shape change (Figure S3D). These results suggest that muscular hydraulics in this reduced system can drive shape change but not cavity inflation.

We performed an shRNA KD screen that targets transcription factors associated with muscle development,[14,40] and we found that the orthogonal organization of the parietal and circular epitheliomuscular cells is severely disrupted in the double KD of *Tbx20* paralogs (*NvTbx20.1* and *NvTbx20.2*) (Figures 5C, S3B, and S3E–S3G). These *Tbx20* KD animals with a disorganized body wall musculature had a wider and shorter body column, displaying a bulky sac-like polyp morphology (Figures 5C and S3G). We independently validated the developmental function of *Tbx20* by simultaneously disrupting both paralogs with the CRISPR-Cas9 system (Figure S3H). F0 *Tbx20* double knockout animals exhibited a nearly spherical morphology resulting from a global disruption of parietal and circular epitheliomuscular cells (Figures S3I–S3K). During development, *Tbx20* KD animals showed normal settlement behaviors (Figures 5F and 5G) and displayed peristaltic waves that correlate with cavity inflation (Figure S4A; Video S7). In agreement with this, the development of *Tbx20* KD larvae was dominated by IE and AE, leading to organismal size increase with a limited increase in aspect ratio (Figures 5D, 5E, and 5H; Video S6). These experiments demonstrate key roles for the *Tbx20* family in controlling parietal and CM patterning and reveal a previously unknown link between the spatial organization of epitheliomuscular cells and organismal shape.

To mimic the passive effects of the constraining parietal (axial) and circular (azimuthal) musculature, we realized simple physical experiments with elastomeric balloons, with and without bands and tapes. By varying the protocols for inflation and reinforcement (Figure S5), we reproduced the morphological patterns of *Tbx20* KD, *BMP2/4* KD, and wild-type animals using balloon mimics (Figure 5E). This further supports that our quantitative physical model, which incorporates static and dynamic pressure components, as well as directionality of the stress (axial versus azimuthal), accurately recapitulates observed changes that accompany larva-polyp morphogenesis. Taken together with earlier results, these findings suggest that the developmental organization of the muscular system is critical for organismal size and shape.

Muscular hydraulics impact tissue remodeling

Next, we examined the relationship between muscular-hydraulics and tissue dynamics. Particularly, we analyzed the response of ectodermal and endodermal cells in the body wall to three distinct muscular-hydraulic pertubations: (1) lack of hydraulic stress in depressurized animals, (2) inflation with defective anisotropy in *Tbx20* KD animals, and (3) AS with minimal inflation in *BMP2/4* KD animals (Figure 6A). At a cellular level, three motifs are distinguished during axial elongation: oriented cell division,

Please cite this article in press as: Stokkermans et al., Muscular hydraulics drive larva-polyp morphogenesis, Current Biology (2022), https://doi.org/10.1016/j.cub.2022.08.065

CellPress
OPEN ACCESS

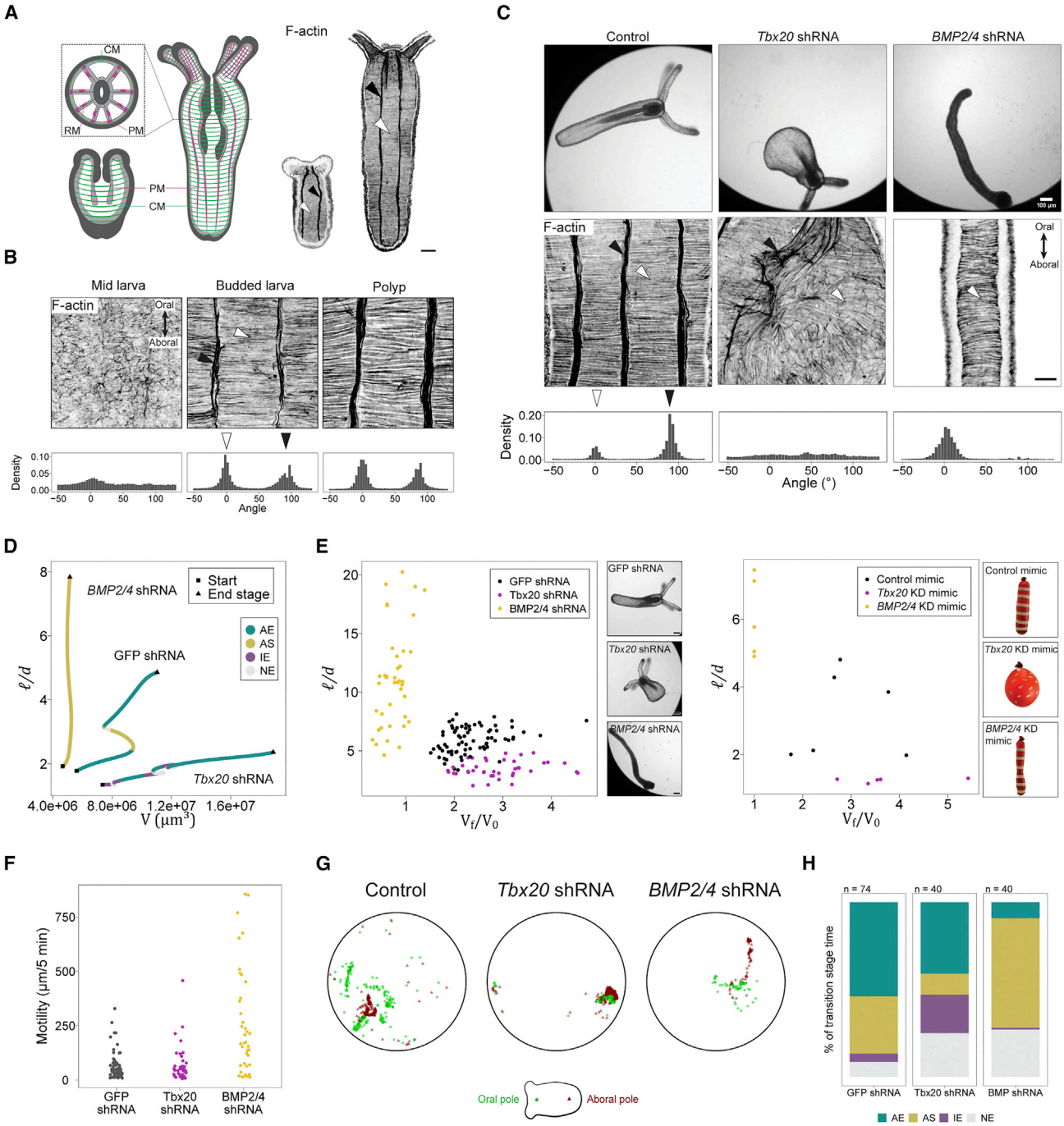

Figure 5. Targeting muscle organization affects body shape and size

(A) Left: the schematic representation of muscle organization. The dotted box shows the cross-sectional view. CM, circular muscle; PM, parietal muscle; RM, retractor muscle. Right: F-actin staining showing parietal (black arrowhead) and circular (white arrowhead) muscles.

(B) Top: muscle organization at different developmental stages. Bottom: distribution of muscle orientations. An angle close to 0° typically indicates circular muscles, and an angle close to 90° indicates longitudinal muscles.

(C) Top: bright-field images of control, *Tbx20* KD, and *BMP2/4* KD animals. Middle: representative confocal images showing muscle organization in each condition. Bottom: the distribution of muscle orientations.

(D) Trajectories in morphospace.

(E) Morphospace plots for body column aspect ratio (ℓ/d) as a function of cavity volume changes (V_f/V_0) for KD animals (left) and balloon (right) experiments.

(F) Quantification of motility.

(legend continued on next page)

cell shape change, and oriented cell rearrangements. Blocking cell proliferation with hydroxyurea during larva-polyp transition had minimal effect on body elongation and tissue volume (Figures S4B–S4E), suggesting that larva-polyp morphogenesis occurs primarily by tissue remodeling.[21] Indeed, a change in cell shape in both tissue layers reduced body wall tissue thickness and increased the cell apical surface area (Figures 6B–6E), leading to an expansion of the entire animal's surface. This decrease in epithelial thickness was blocked in depressurized larvae, reinforcing the importance of muscular hydraulics in the remodeling of the body wall tissue. Interestingly, ectodermal cells in depressurized larvae also did not differentiate the apical actin-enriched rings that typically surround cilia,[41] which suggests that the disruption of cavity pressure delays or arrests epidermal cell differentiation (Figure S4F). *BMP2/4* KD animals also showed a moderate reduction in body wall thickness compared with controls and *Tbx20* KD (Figure 6D). This could be explained by the direct involvement of *BMP2/4* signaling in this process and/or the minimal cavity inflation in *BMP2/4* KD animals. Although cell shape changes increase the surface area of the animals, oriented cell rearrangements accounted for the directional expansion along the oral-aboral axis, as visualized by tracking the remodeling of photo-converted Kaede-positive ectodermal stripes along the main body axis (Figure 6F). In *BMP2/4* KD animals, we observed extensive oriented cell rearrangements along the main axis (Figure 6F). By contrast, *Tbx20* KD animals showed reduced cell rearrangements along the main axis (Figure 6F). These patterns of tissue remodeling mirrored the anisotropic and isotropic stresses in *BMP2/4* KD and *Tbx20* KD animals, respectively. Therefore, these findings show a strong link between the developmental behavior of muscular hydraulics and the morphogenetic responses of the body wall.

DISCUSSION

Understanding morphogenesis requires integrating molecular and cellular processes with large-scale active deformations at the organismal level. In particular, hydraulic forces have recently been implicated in a number of early morphogenetic events in cellular cysts,[44] otic vesicles,[45] and whole embryos.[32] In parallel, local muscle contractility is emerging as a key developmental player for many biological systems, including the gut,[46–48] heart,[49] bone,[50,51] lung,[52] whole embryos,[53,54] and wound healing and regeneration.[34,55] Here, we established the critical role of muscular hydraulics in larva-polyp transition in a sea anemone. During development, larvae acquire a primordial hydrostatic skeleton. This hydraulic system generates reversible body deformations through peristaltic waves, squeezing, and longitudinal contractions. Although it remains very difficult to make predictions for long timescale changes based on these short-lived behaviors, mapping body deformations helps to qualitatively link contractions to morphogenesis. As peristaltic waves correlate with volume increase and blocking body contractions prevented cavity inflation, we propose that these coordinated body wall deformations can drive fluid uptake via the oral opening due to suction.[30,56] This scenario would depend on the coordination of mouth opening and closing, which requires further investigation. Based on the perforated capillary experiment, larvae require a pressurized cavity for body elongation. Thus, over longer times, muscle organization in concert with the luminal pressure changes body size and shape by imposing mechanical stress on the body wall leading to large-scale tissue remodeling. However, the molecular mechanisms that translate muscular hydraulics into tissue remodeling through cell shape change and rearrangement are still unknown and require further studies to integrate the dynamics of cell-cell and cell-extracellular matrix interactions in larva-polyp morphogenesis.

We described an unexpected variability in motility behavior and elongation dynamics. Although the genetic and/or developmental origins of this variability are still unknown, a high variation in behavior may provide an advantage to a species under unpredictable environmental conditions, since it increases the chance that some individuals will be well-matched to survive.[57] Under natural conditions, the advantage of early settlement and fast larva-polyp transition would be that the animal might gain the ability to feed earlier. However, prolonged motility might be advantageous under conditions where the local environment is sub-optimal for polyp life, and a better environment might be found elsewhere. As *Nematostella* is a burrowing sea anemone,[58] an alternative hypothesis is that the primary function of peristalsis during larva-polyp transition is predator avoidance by burrowing while secondarily leading to body elongation. In this context, the high motility behavior in a group of settled larvae might be due to the lack of adequate burrowing substrate during imaging. However, our work also showed that a stable sessile adhesion at the aboral pole coincides with a morphodynamical shift from AE to AS. This pattern was not observed in motile animals, which exhibited frequent longitudinal contractions. We identified a clear distinction in contraction behavior between sessile and motile animals, coinciding with different elongation dynamics and shape changes. However, differences in fluid uptake rates and wall mechanical properties might also contribute to the variability in the morphodynamics of body elongation.

The ubiquity of hydrostatic skeletons in the animal kingdom[29] and especially in marine invertebrates suggests a broad role for active muscular hydraulics on their developmental dynamics and sets the stage for the study of the neuro-mechanical control of morphogenesis in organisms and mapping the behavioral dynamics and morphologies across species. In many engineered systems, hydraulics is defined by the ability to harness pressure and flow into mechanical work, with long-range effects in space-time. As animal multicellularity evolved in an aquatic environment, we propose that early animals likely exploited the same physics, with hydraulics underlying both developmental and behavioral decisions.

(G) Positions of the oral (green dot) and aboral (red triangle) pole.
(H) Bar plot showing the percentage of transition stage time spent in the different categories of morphodynamics for each KD condition.
Scale bars: 50 μm in (A), 10 μm in (B), 100 μm in (C, top), and 20 μm in (C, middle).
See also Figures S3, S4, and S5 and Videos S6 and S7.

Please cite this article in press as: Stokkermans et al., Muscular hydraulics drive larva-polyp morphogenesis, Current Biology (2022), https://doi.org/10.1016/j.cub.2022.08.065

CellPress
OPEN ACCESS

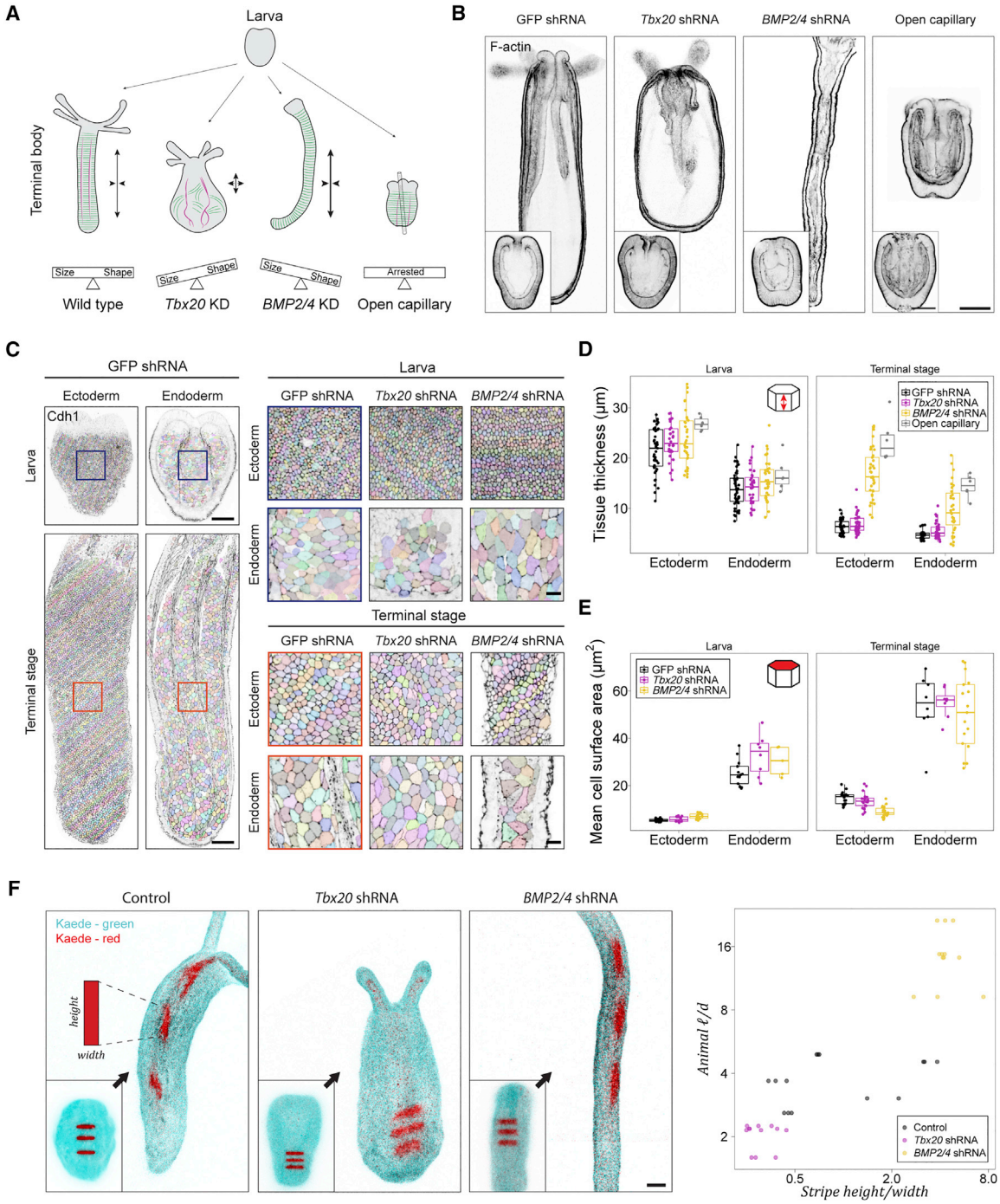

Figure 6. The cellular dynamics in the body wall depend on muscular hydraulics

(A) Schematic representation of muscle organization and animal shape-size relationship for all perturbations.

(B) Mid-plane slices of animals stained for F-actin. Insets show larvae.

(C) Ectodermal and endodermal surface view for animals stained for cadherin3 (panels for the larva of *Tbx20* KD and *BMP2/4* KD) or cadherin1 (all other panels).[42] Colors indicate cell segmentation (Cellpose[43]).

(D) Quantification of tissue thickness for the ectoderm and endoderm epithelial layers.

(E) Quantification of mean cell apical surface area for ectoderm and endoderm at larval and terminal stage.

(F) Photo-converted horizontal tissue stripes in larvae expressing Kaede (cyan: not converted; red: photo-converted) and their corresponding topological changes in each KD condition. The plot on the right shows the stripe length/width aspect ratio versus the animal body column aspect ratio at the terminal stage. n = 5 (GFP KD), n = 4 (*Tbx20* KD), and n = 4 (*BMP2/4* KD).

Scale bars: 100 µm in (B), 50 µm in (C, overview), 10 µm in (C, zoom), and 50 µm in (F).

See also Figure S4.

STAR★METHODS

Detailed methods are provided in the online version of this paper and include the following:

- KEY RESOURCES TABLE
- RESOURCE AVAILABILITY
  - Lead contact
  - Materials availability
  - Data and code availability
- EXPERIMENTAL MODEL AND SUBJECT DETAILS
- METHOD DETAILS
  - High-throughput live imaging
  - Image analysis of live animals
  - Optical coherence microscopy and data processing
  - Pressure measurements
  - Pharmacological treatments
  - Fixation and immunostaining
  - Confocal imaging
  - Quantification of cellular properties
  - shRNA design and synthesis
  - Microinjection of shRNAs
  - Quantification of *Tbx20* expression after shRNA knockdown
  - CRISPR/Cas9
  - Genotyping of *Tbx20* F0 animals
  - Photoconversion of Kaede
  - Biophysical manipulation
  - Biophysical model
  - Physical balloon experiments
- QUANTIFICATION AND STATISTICAL ANALYSIS

SUPPLEMENTAL INFORMATION

Supplemental information can be found online at https://doi.org/10.1016/j.cub.2022.08.065.

ACKNOWLEDGMENTS

We thank the members of the ALMF at EMBL for the imaging support. We also thank all the DB group leaders at EMBL for their comments on the manuscript. K.S. is supported by the EIPOD under the Marie Curie co-fund actions MSCA co-fund FP664726. R.P. is supported by an ERC Consolidator Grant (no. 864027, Brillouin4Life). This work was supported by the NSF-Simons Center for Quantitative Biology at Harvard University (L.M.), the Simons Foundation (L.M.), the Henri Seydoux Fund (L.M.), and the European Molecular Biology Laboratory (A.I.).

AUTHOR CONTRIBUTIONS

A.S. and A.I. conceived the idea for this project and designed most of the experiments. A.C. and L.M. designed, generated, and integrated the theoretical and physical models with the biophysical experiments. A.S. established the high-throughput live imaging and computational pipeline for image analyses with support from G.M. A.S. performed the shRNA KDs, pharmacological treatments, staining, photoconversion, and all imaging and data quantification. A.I. performed the capillary experiments and CRISPR-Cas9 mutagenesis. P.M. measured the cavity pressure under T.H.'s supervision. L.W. and R.P. designed, built, and optimized the dual-view optical coherence microscopy (OCM). K.S. acquired the OCM images, and L.W., K.S., and A.S. performed the image data processing. A.C. conducted the physical experiments with balloons. L.M. outlined the theoretical framework. S.Y. carried out simulations of the theoretical model. P.S. optimized the pharmacological experiments. A.I. drafted the manuscript with inputs from A.S., A.C., and L.M. All authors edited the manuscript.

DECLARATION OF INTERESTS

The authors declare no competing interests.

Received: October 1, 2021
Revised: July 14, 2022
Accepted: August 22, 2022
Published: September 16, 2022

REFERENCES

1. Lecuit, T., and Mahadevan, L. (2017). Morphogenesis one century after on growth and form. Development *144*, 4197–4198.
2. Mahadevan, L. (2020). Multicellular morphogenesis. In Proceedings of the 27th Solvay Conference on Physics (2017) - PHYSICS OF LIVING MATTER: space, time and information, D. Gross, and B. Shraiman, eds. (World Scientific).
3. Murrell, M., Oakes, P.W., Lenz, M., and Gardel, M.L. (2015). Forcing cells into shape: the mechanics of actomyosin contractility. Nat. Rev. Mol. Cell Biol. *16*, 486–498.
4. Mishra, N., and Heisenberg, C.P. (2021). Dissecting organismal morphogenesis by bridging genetics and biophysics. Annu. Rev. Genet. *55*, 209–233.
5. Krzic, U., Gunther, S., Saunders, T.E., Streichan, S.J., and Hufnagel, L. (2012). Multiview light-sheet microscope for rapid in toto imaging. Nat. Methods *9*, 730–733.
6. Yue, Y., Zong, W., Li, X., Li, J., Zhang, Y., Wu, R., Liu, Y., Cui, J., Wang, Q., Bian, Y., et al. (2020). Long-term, in toto live imaging of cardiomyocyte behaviour during mouse ventricle chamber formation at single-cell resolution. Nat. Cell Biol. *22*, 332–340.
7. Collinet, C., and Lecuit, T. (2021). Programmed and self-organized flow of information during morphogenesis. Nat. Rev. Mol. Cell Biol. *22*, 245–265.
8. Stooke-Vaughan, G.A., and Campàs, O. (2018). Physical control of tissue morphogenesis across scales. Curr. Opin. Genet. Dev. *51*, 111–119.
9. Heisenberg, C.P., and Bellaïche, Y. (2013). Forces in tissue morphogenesis and patterning. Cell *153*, 948–962.
10. Branson, K., Robie, A.A., Bender, J., Perona, P., and Dickinson, M.H. (2009). High-throughput ethomics in large groups of Drosophila. Nat. Methods *6*, 451–457.
11. Mearns, D.S., Donovan, J.C., Fernandes, A.M., Semmelhack, J.L., and Baier, H. (2020). Deconstructing hunting behavior reveals a tightly coupled stimulus-response loop. Curr. Biol. *30*, 54–69.e9.
12. Layden, M.J., Rentzsch, F., and Röttinger, E. (2016). The rise of the starlet sea anemone Nematostella vectensis as a model system to investigate development and regeneration. Wiley Interdiscip. Rev. Dev. Biol. *5*, 408–428.
13. Martindale, M.Q., Pang, K., and Finnerty, J.R. (2004). Investigating the origins of triploblasty: "mesodermal" gene expression in a diploblastic animal, the sea anemone Nematostella vectensis (phylum, Cnidaria; class, Anthozoa). Development *131*, 2463–2474.
14. Steinmetz, P.R.H.H., Aman, A., Kraus, J.E.M.M., and Technau, U. (2017). Gut-like ectodermal tissue in a sea anemone challenges germ layer homology. Nat. Ecol. Evol. *1*, 1535–1542.
15. Technau, U., and Steele, R.E. (2012). Evolutionary crossroads in developmental biology: Cnidaria. Development *138*, 4491.
16. Müller, W.A., and Leitz, T. (2002). Metamorphosis in the Cnidaria. Can. J. Zool. *80*, 1755–1771.
17. Grasso, L.C., Negri, A.P., Fôret, S., Saint, R., Hayward, D.C., Miller, D.J., and Ball, E.E. (2011). The biology of coral metamorphosis: molecular responses of larvae to inducers of settlement and metamorphosis. Dev. Biol. *353*, 411–419.

18. Seipp, S., Schmich, J., and Leitz, T. (2001). Apoptosis – a death-inducing mechanism tightly linked with morphogenesis in Hydractina echinata (Cnidaria, Hydrozoa). Development *128*, 4891–4898.
19. Plickert, G., Kroiher, M., and Munck, A. (1988). Cell proliferation and early differentiation during embryonic development and metamorphosis of Hydractinia echinata. Development *103*, 795–803.
20. Krasovec, G., Pottin, K., Rosello, M., Quéinnec, É., and Chambon, J.P. (2021). Apoptosis and cell proliferation during metamorphosis of the planula larva of Clytia hemisphaerica (Hydrozoa, Cnidaria). Dev. Dyn. *250*, 1739–1758.
21. Fritz, A.E., Ikmi, A., Seidel, C., Paulson, A., and Gibson, M.C. (2013). Mechanisms of tentacle morphogenesis in the sea anemone Nematostella vectensis. Development *140*, 2212–2223.
22. Hand, C., and Uhlinger, K.R. (1992). The culture, sexual and asexual reproduction, and growth of the sea anemone Nematostella vectensis. Biol. Bull. *182*, 169–176.
23. Yamashita, K., Kawaii, S., Nakai, M., and Fusetani, N. (2003). Larval behavioral, morphological changes, and nematocyte dynamics during settlement of actinulae of Tubularia mesembryanthemum, Allman 1871 (Hydrozoa: Tubulariidae). Biol. Bull. *204*, 256–269.
24. Renfer, E., and Technau, U. (2017). Meganuclease-assisted generation of stable transgenics in the sea anemone Nematostella vectensis. Nat. Protoc. *12*, 1844–1854.
25. Ikmi, A., McKinney, S.A., Delventhal, K.M., Gibson, M.C., and Stuurman, N. (2014). TALEN and CRISPR/Cas9-mediated genome editing in the early-branching metazoan Nematostella vectensis. Nat. Commun. *5*, 5486.
26. He, S., Del Viso, F., Chen, C.Y., Ikmi, A., Kroesen, A.E., and Gibson, M.C. (2018). An axial Hox code controls tissue segmentation and body patterning in Nematostella vectensis. Science *361*, 1377–1380.
27. Leitz, T. (1997). Induction of settlement and metamorphosis of cnidarian larvae: signals and signal transduction. Invertebr. Reprod. Dev. *31*, 109–122.
28. Jackson, D., Leys, S.P., Hinman, V.F., Woods, R., Lavin, M.F., and Degnan, B.M. (2002). Ecological regulation of development: induction of marine invertebrate metamorphosis. Int. J. Dev. Biol. *46*, 679–686.
29. Kier, W.M. (2012). The diversity of hydrostatic skeletons. J. Exp. Biol. *215*, 1247–1257.
30. Batham, E.J., and Pantin, C.F. (1950). Muscular and hydrostatic action in the sea-anemone Metridium senile (L.). J. Exp. Biol. *27*, 264–289.
31. Batham, E.J., and Pantin, C.F. (1951). The organization of the muscular system of Metridium senile. Q. J. Microsc. Sci. *92*, 27–54.
32. Chan, C.J., Costanzo, M., Ruiz-Herrero, T., Mönke, G., Petrie, R.J., Bergert, M., Diz-Muñoz, A., Mahadevan, L., and Hiiragi, T. (2019). Hydraulic control of mammalian embryo size and cell fate. Nature *571*, 112–116.
33. Petrie, R.J., Koo, H., and Yamada, K.M. (2014). Generation of compartmentalized pressure by a nuclear piston governs cell motility in a 3D matrix. Science *345*, 1062–1065.
34. Abrams, M.J., Basinger, T., Yuan, W., Guo, C.-L., and Goentoro, L. (2015). Self-repairing symmetry in jellyfish through mechanically driven reorganization. Proc. Natl. Acad. Sci. USA *112*, E3365–E3373.
35. Goel, T., Wang, R., Martin, S., Lanphear, E., and Collins, E.-M.S. (2019). Linalool acts as a fast and reversible anesthetic in Hydra. PloS One *14*, 584946.
36. Alexander, R.M. (1962). Viso-elastic properties of the body-wall of sea anemones. J. Exp. Biol. *39*, 373–386.
37. Jahnel, S.M., Walzl, M., and Technau, U. (2014). Development and epithelial organisation of muscle cells in the sea anemone Nematostella vectensis. Front. Zool. *11*, 44.
38. Leclère, L., and Rentzsch, F. (2014). RGM regulates BMP-mediated secondary axis formation in the sea anemone Nematostella vectensis. Cell Rep *9*, 1921–1930.
39. Saina, M., Genikhovich, G., Renfer, E., and Technau, U. (2009). BMPs and chordin regulate patterning of the directive axis in a sea anemone. Proc. Natl. Acad. Sci. USA *106*, 18592–18597.
40. Sebé-Pedrós, A., Saudemont, B., Chomsky, E., Plessier, F., Mailhé, M.P., Renno, J., Loe-Mie, Y., Lifshitz, A., Mukamel, Z., Schmutz, S., et al. (2018). Cnidarian cell type diversity and regulation revealed by whole-organism single-cell RNA-seq. Cell *173*, 1520–1534.e20.
41. Momose, T., Kraus, Y., Houliston, E., Kraus, T.M.Y., and Houliston, E. (2012). A conserved function for Strabismus in establishing planar cell polarity in the ciliated ectoderm during cnidarian larval development. Development *139*, 4374–4382.
42. Pukhlyakova, E.A., Kirillova, A.O., Kraus, Y.A., Zimmermann, B., and Technau, U. (2019). A cadherin switch marks germ layer formation in the diploblastic sea anemone Nematostella vectensis. Development *146*, dev174623.
43. Stringer, C., Wang, T., Michaelos, M., and Pachitariu, M. (2021). Cellpose: a generalist algorithm for cellular segmentation. Nat. Methods *18*, 100–106.
44. Ruiz-Herrero, T., Alessandri, K., Gurchenkov, B.V., Nassoy, P., and Mahadevan, L. (2017). Organ size control via hydraulically gated oscillations. Development *144*, 4422–4427.
45. Mosaliganti, K.R., Swinburne, I.A., Chan, C.U., Obholzer, N.D., Green, A.A., Tanksale, S., Mahadevan, L., and Megason, S.G. (2019). Size control of the inner ear via hydraulic feedback. eLife *8*.
46. Shyer, A.E., Huycke, T.R., Lee, C., Mahadevan, L., and Tabin, C.J. (2015). Bending Gradients: how the intestinal stem cell gets its home. Cell *161*, 569–580.
47. Khalipina, D., Kaga, Y., Dacher, N., and Chevalier, N.R. (2019). Smooth muscle contractility causes the gut to grow anisotropically. J. R. Soc. Interface *16*, 20190484.
48. Huycke, T.R., Miller, B.M., Gill, H.K., Nerurkar, N.L., Sprinzak, D., Mahadevan, L., and Tabin, C.J. (2019). Genetic and mechanical regulation of intestinal smooth muscle development. Cell *179*, 90–105.e21.
49. Majkut, S., Dingal, P.C.D.P., and Discher, D.E. (2014). Stress sensitivity and mechanotransduction during heart development. Curr. Biol. *24*, R495–R501.
50. Felsenthal, N., and Zelzer, E. (2017). Mechanical regulation of musculoskeletal system development. Development *144*, 4271–4283.
51. Schwartz, A.G., Lipner, J.H., Pasteris, J.D., Genin, G.M., and Thomopoulos, S. (2013). Muscle loading is necessary for the formation of a functional tendon enthesis. Bone *55*, 44–51.
52. Kim, H.Y.Y., Pang, M.-F.F., Varner, V.D., Kojima, L., Miller, E., Radisky, D.C.C., and Nelson, C.M.M. (2015). Localized smooth muscle differentiation is essential for epithelial bifurcation during branching morphogenesis of the mammalian lung. Dev. Cell *34*, 719–726.
53. Lardennois, A., Pásti, G., Ferraro, T., Llense, F., Mahou, P., Pontabry, J., Rodriguez, D., Kim, S., Ono, S., Beaurepaire, E., et al. (2019). An actin-based viscoplastic lock ensures progressive body-axis elongation. Nature *573*, 266–270.
54. Zhang, H., Landmann, F., Zahreddine, H., Rodriguez, D., Koch, M., and Labouesse, M. (2011). A tension-induced mechanotransduction pathway promotes epithelial morphogenesis. Nature *471*, 99–103.
55. Livshits, A., Shani-Zerbib, L., Maroudas-Sacks, Y., Braun, E., and Keren, K. (2017). Structural inheritance of the actin cytoskeletal organization determines the body axis in regenerating Hydra. Cell Rep *18*, 1410–1421.
56. Vogel, S. (2007). Living in a physical world X. Pumping fluids through conduits. J. Biosci. *32*, 207–222.
57. Honegger, K., and de Bivort, B. (2018). Stochasticity, individuality and behavior. Curr. Biol. *28*, R8–R12.
58. Williams, R.B. (2003). Locomotory behaviour and functional morphology of Nematostella vectensis (Anthozoa: Actiniaria: Edwardsiidae): a contribution to a comparative study of burrowing behaviour in athenarian sea. anemones.Zoologische *345*, 437–484.

59. Putnam, N.H., Srivastava, M., Hellsten, U., Dirks, B., Chapman, J., Salamov, A., Terry, A., Shapiro, H., Lindquist, E., Kapitonov, V.V., et al. (2007). Sea anemone genome reveals ancestral eumetazoan gene repertoire and genomic organization. Science *317*, 86–94.
60. Schindelin, J., Arganda-Carreras, I., Frise, E., Kaynig, V., Longair, M., Pietzsch, T., Preibisch, S., Rueden, C., Saalfeld, S., Schmid, B., et al. (2012). Fiji: an open-source platform for biological-image analysis. Nat. Methods *9*, 676–682.
61. Arganda-Carreras, I., Fernández-González, R., Muñoz-Barrutia, A., and Ortiz-de-Solorzano, C. (2010). 3D reconstruction of histological sections: application to mammary gland tissue. Microsc. Res. Tech. *73*, 1019–1029.
62. Legland, D., Arganda-Carreras, I., and Andrey, P. (2016). MorphoLibJ: integrated library and plugins for mathematical morphology with ImageJ. Bioinformatics *32*, 3532–3534.
63. Linkert, M., Rueden, C.T., Allan, C., Burel, J.M., Moore, W., Patterson, A., Loranger, B., Moore, J., Neves, C., MacDonald, D., et al. (2010). Metadata matters: access to image data in the real world. J. Cell Biol. *189*, 777–782.
64. Li, K., Wu, X., Chen, D.Z., and Sonka, M. (2006). Optimal surface segmentation in volumetric images - A graph-theoretic approach. IEEE Trans. Pattern Anal. Mach. Intell. *28*, 119–134.
65. Fernandez, R., and Moisy, C. (2021). Fijiyama: A registration tool for 3D multimodal time-lapse imaging. Bioinformatics *37*, 1482–1484.
66. Arganda-Carreras, I., Kaynig, V., Rueden, C., Eliceiri, K.W., Schindelin, J., Cardona, A., and Sebastian Seung, H.S. (2017). Trainable Weka Segmentation: a machine learning tool for microscopy pixel classification. Bioinformatics *33*, 2424–2426.
67. Labun, K., Montague, T.G., Krause, M., Torres Cleuren, Y.N., Tjeldnes, H., and Valen, E. (2019). CHOPCHOP v3: expanding the CRISPR web toolbox beyond genome editing. Nucleic Acids Res *47*, W171–W174.
68. Mönke, G., Sorgenfrei, F.A., Schmal, C., and Granada, A.E. (2020). Optimal time frequency analysis for biological data - pyBOAT. Preprint at bioRxiv. https://doi.org/10.1101/2020.04.29.067744.
69. Ando, R., Hama, H., Yamamoto-Hino, M., Mizuno, H., and Miyawaki, A. (2002). An optical marker based on the UV-induced green-to-red photoconversion of a fluorescent protein. Proc. Natl. Acad. Sci. USA *99*, 12651–12656.
70. R Core Team (2019). R: A Language and Environment for Statistical Computing (R Foundation for Statistical Computing).
71. RStudio Team (2015). RStudio (Integrated Development Environment for R). http://www.rstudio.com/.
72. Wickham, H., Averick, M., Bryan, J., Chang, W., McGowan, L.D., François, R., Grolemund, G., Hayes, A., Henry, L., Hester, J., et al. (2019). Welcome to the tidyverse. J. Open Source Softw. *4*, 1686.
73. Wickham, H. (2009). ggplot2 (Springer).
74. Kassambara, A. (2020). Ggpubr: "ggplot2" Based Publication Ready Plots. https://rpkgs.datanovia.com/ggpubr/.
75. Wickham, H., and Pedersen, T.L. (2019). gtable: arrange "Grobs". In Tables.
76. Petukhov, V., van den Brand, T., and Biederstedt, E. (2020). Ggrastr: Raster Layers for "ggplot2. https://CRAN.R-project.org/package=*ggrastr*.
77. Hyndman, R.J., Athanasopoulos, G., Bergmeir, C., Caceres, G., Chhay, L., O'Hara-Wild, M., Petropoulos, F., and Razbash, S. (2020). Package 'forecast. https: //cran. r-project. org/web/packages/forecast/forecast. pdf.
78. Hyndman, R.J., and Khandakar, Y. (2008). Automatic time series forecasting: the forecast package for R. J. Stat. Softw. *27*, 1–22.
79. Genikhovich, G., and Technau, U. (2009). Induction of spawning in the starlet sea anemone Nematostella vectensis, in vitro fertilization of gametes, and Dejellying of zygotes. Cold Spring Harb. Protoc. *2009*. pdb.prot5281.
80. Drexler, W., and Fujimoto, J.G. (2015). In Optical Coherence Tomography: Technology and Applications, Second Edition, W. Drexler, and J.G. Fujimoto, eds. (Springer International Publishing).
81. Lan, G., and Li, G. (2017). Design of a k-space spectrometer for ultra-broad waveband spectral domain optical coherence tomography. Sci. Rep. *7*, 42353.
82. Liba, O., Sorelle, E.D., Sen, D., and de la Zerda, A. De. (2016). Contrast-enhanced optical coherence tomography with picomolar sensitivity for functional in vivo imaging. Sci. Rep. *6*, 23337.
83. Berg, S., Kutra, D., Kroeger, T., Straehle, C.N., Kausler, B.X., Haubold, C., Schiegg, M., Ales, J., Beier, T., Rudy, M., et al. (2019). ilastik: interactive machine learning for (bio)image analysis. Nat. Methods *16*, 1226–1232.
84. Khuenl-Brady, K.S., and Sparr, H. (1996). Clinical pharmacokinetics of rocuronium bromide. Clin. Pharmacokinet. *31*, 174–183.
85. Chen, C.Y., McKinney, S.A., Ellington, L.R., and Gibson, M.C. (2020). Hedgehog signaling is required for endomesodermal patterning and germ cell development in the sea anemone Nematostella vectensis. eLife *9*, 1–27.
86. Fishman, A., Light, D., and Lamm, A.T. (2018). QsRNA-seq: a method for high-throughput profiling and quantifying small RNAs. Genome Biol *19*, 113.
87. Xie, F., Xiao, P., Chen, D., Xu, L., and Zhang, B. (2012). miRDeepFinder: A miRNA analysis tool for deep sequencing of plant small RNAs. Plant Mol. Biol. *80*, 75–84.
88. McMahon, T.A. (2020). Muscles, Reflexes, and Locomotion (Princeton University Press).

Please cite this article in press as: Stokkermans et al., Muscular hydraulics drive larva-polyp morphogenesis, Current Biology (2022), https://doi.org/10.1016/j.cub.2022.08.065

CellPress
OPEN ACCESS

STAR★METHODS

KEY RESOURCES TABLE

REAGENT or RESOURCE	SOURCE	IDENTIFIER
Antibodies		
Mouse anti cadherin3 antibody	Technau lab	Pukhlyakova et al.[42]
Mouse anti phosphorylated histone 3 antibody	Sigma	Cat#05-806; RRID:AB_310016
Donkey-anti-mouse Alexa Fluor 488	ThermoFisher	Cat#A21202; RRID:AB_141607
Goat-anti-mouse Alexa Fluor 488	ThermoFisher	Cat#A11001; RRID:AB_2534069
Chemicals, peptides, and recombinant proteins		
Hydroxy Urea	Sigma	h8627
Linalool	Sigma	L2602
Menthol	Sigma	M2772
Rocuronium bromide	Sigma	R5155
Recombinant Cas9 protein	PNA bio	CP01-20
FITC	ThermoFisher	46425
Texas Red-labelled Dextran	ThermoFisher	D3328
Hoechst 34580	Sigma	63493
phalloidin Alexa Fluor 546	ThermoFisher	A22283
Critical commercial assays		
T7 MegaShortScript kit	Invitrogen	AM1354
HiScribe™ T7 ARCA mRNA Kit (with tailing)	NEB	E2060S
Experimental models: Organisms/strains		
Nematostella vectensis	Martindale lab	Putnam et al.[59]
Oligonucleotides		
Primer GFP shRNA (forward) TAATACGACTCACTATAG GGGCACAAGCTGGAGTAC AATTCAAGAGATTGTACTC CAGCTTGTGCCCTT	This paper	N/A
Primer GFP shRNA (reverse) AAGGGCACAAGCTGGAGT ACAATCTCTTGAATTGTAC TCCAGCTTGTGCCCCTAT AGTGAGTCGTATTA	This paper	N/A
Primer Tbx20 shRNA (forward) TAATACGACTCACTATAGGG AACAGCTGCTTAAACATTCAA GAGATGTTTAAGCAGCTGTTC CCTT	This paper	N/A
Primer Tbx20 shRNA (reverse) AAGGGAACAGCTGCTTAAAC ATCTCTTGAATGTTTAAGCAG CTGTTCCCTATAGTGAGTCG TATTA	This paper	N/A
Primer BMP shRNA (forward) TAATACGACTCACTATAGGA CTGGATATTCAAGTGATTCA AGAGATCACTTGAATATCCA GTCCTT	This paper	N/A

(*Continued on next page*)

Continued

REAGENT or RESOURCE	SOURCE	IDENTIFIER
Primer BMP shRNA (reverse) AAGGACTGGATATTCAAGT GATCTCTTGAATCACTTGA ATATCCAGTCCTATAGTGA GTCGTATTA	This paper	N/A
Tbx20 sgRNA-1: ACGTTGC GGATCTCCGTGAGTGG	This paper	N/A
Tbx20 sgRNA-2: CCCTGACT CACCGTTCACGGGGG	This paper	N/A
PCR amplification of Kaede (forward) TAATACGACTCA CTATAGGGCCACCATGGT GAGTCTG	This paper	N/A
PCR amplification of Kaede (reverse) TAAGATACATTGAT GAGTTTGGACAAACCACAAC TAGAAT	This paper	N/A
Recombinant DNA		
Kaede-NLS plasmid	Gift from Michael Davidson	addgene, 57319
Software and algorithms		
FIJI	Schindelin et al.[60]	https://imagej.net/software/fiji/
FIJI plugins: AnalyzeSkeleton plugin MorpholibJ BioFormats plugin VolumeViewer Minimum Cost Z surface Projection Fijiyama Weka segmentation	Arganda-Carreras et al.[61] Legland et al.[62] Linkertet al.[63] Kai Uwe Barthel Li et al.[64] Fernandez and Moisy[65] Arganda-Carreras et al.[66]	https://imagej.net/plugins/analyze-skeleton/ https://imagej.net/plugins/morpholibj https://www.openmicroscopy.org/bio-formats/ https://imagej.nih.gov/ij/plugins/volume-viewer.html https://imagej.net/plugins/minimum-cost-z-surface-projection https://imagej.net/plugins/fijiyama https://imagej.net/plugins/tws/
siRNA Wizard	Invivogen	https://www.invivogen.com/sirnawizard/design_advanced.php
Chopchop	Labun et al.[67]	http://chopchop.cbu.uib.no
PyBOAT (v0.9.8)	Mönke et al.[68]	https://github.com/tensionhead/pyBOAT
Cellpose (cyto model)	Ando et al.[69]	https://github.com/MouseLand/cellpose
RStudio version 1.1.442	R Core Team[70] and RStudio Team[71]	https://www.rstudio.com/
R packages: tidyverse ggplot2 ggpubr gtable ggrastr forecast	Wickham et al.[72] Wickham[73] Kassambara[74] Wickham and Pedersen[75] Petukhov et al.[76] Hyndman et al.[77] and Hyndman and Khandakar[78]	https://cran.r-project.org/web/packages/
Prism8	Graphpad	https://www.graphpad.com/scientific-software/prism/
Other		
Latex balloons	Celebrate It™	10108443
elastic braided bands	Loops & Threads™	10187887
inextensible electrical tapes	Gardner Bender	GTW-667P
stretchable adhesive	Loctite vinyl fabric & plastic flexible adhesive	1360694

Please cite this article in press as: Stokkermans et al., Muscular hydraulics drive larva-polyp morphogenesis, Current Biology (2022), https://doi.org/10.1016/j.cub.2022.08.065

CellPress
OPEN ACCESS

RESOURCE AVAILABILITY

Lead contact

Further information and requests for resources and reagents should be directed to and will be fulfilled by the lead contact, Aissam Ikmi (aissam.ikmi@embl.de).

Materials availability

This study did not generate new unique reagents.

Data and code availability

- The authors declare that all data supporting the findings of this study are available within the manuscript and its supplementary files. Raw data will be shared by the lead contact upon request.
- This paper does not report original code.
- Any additional information required to reanalyze the data reported in this paper is available from the lead contact upon request.

EXPERIMENTAL MODEL AND SUBJECT DETAILS

Nematostella adults[59] were spawned every 3 weeks, and were maintained in a circulating system with 12 parts per thousand (ppt) artificial seawater (ASW) (sea salt; instant ocean) at 17 °C in the dark. Spawning was induced in a light box using a temperature of 28 °C and light intensity of 250–300 lumen per square foot for about approximately 6 hours.[79] Spawning occurred within 3–4 h after a cold-water change (17 °C).

METHOD DETAILS

High-throughput live imaging

Larvae were placed in a 384 well plate (Corning, 3540) using a glass mouth pipet, and each well contained a single larva in 25 μl 12 ppt ASW. The plate was imaged using an Acquifer screening microscope with a 4x magnification objective, with brightfield channel (20% intensity), at 5-minute time resolution at 27 °C for 3-7 days. For high-time resolution recordings, the time interval was 5 seconds.

Image analysis of live animals

All image analyses were performed in FIJI (https://imagej.net/software/fiji/).[60] Development of live animals was analyzed using a Jython script written to run in FIJI. The script segments the animal and identifies the main body axis and secondary branches (tentacles), using the AnalyzeSkeleton plugin.[61] Body length is defined by the main skeleton branch, plus a correction at the oral and aboral extremities based on the Euclidean distance map of the segmented animal. Animal body column diameter is calculated from the distance from each point along the main body axis to the boundary of the animal using FIJI's Euclidean distance map function (body column diameter = distance from skeleton midline to boundary * 2). The volume is estimated by taking the sum of the volumes of 1-pixel tall cylinders with a diameter determined by the local body column diameter, plus two half-spheres to account for the two poles. The script also makes use of the MorphoLibJ package[62] and the BioFormats plugin.[63] The windowed sinc-filter from the pyBOAT package (v0.9.8),[68] with cut-off periods of 500 and 1000 minutes was used to smooth the 5-minute time resolution data. This removes all high frequency components and leaves only the main trend intact. Staging of the animals was based on the decrease in circularity of the segmented 2D shape of the animal, due to elongation of the body column and outgrowth of tentacles. Circularity is defined as $4\pi(\text{area}/\text{perimeter}^2)$, where a value of 1 corresponds to a perfect circle. A threshold of 0.8 for smoothed circularity, using a cut-off period of 1000 minutes, was used to mark the boundary between larva and the larva-polyp transition. Similarly, a threshold of 0.3 marked the boundary between animals undergoing larva-polyp transition and polyps. For shRNA-injected animals, this staging method was refined to include body column volume and aspect ratio using the following thresholds: larva – transition: circularity: 0.8, aspect ratio: 1.8, body column volume: $0.75*10^7$ μm^3; transition – polyp: circularity: 0.3. aspect ratio: 7, body column volume $1.8*10^7$ μm^3.

To define different morphodynamics, the derivatives of the smoothed aspect ratio and estimated body column volume (cut-off period of 500 minutes for 5-minute time resolution data) were used. The values were truncated and normalized to the 95th percentile for aspect ratio and volume change. This way, all values are scored between -1 and 1, where 0 means no change and 1 corresponds to the value of the 95th percentile. Negative scores indicate a decrease in aspect ratio or volume. To define the different morphodynamics, a cut-off value of +0.2 was used, such that axial stretching is defined by a normalized aspect ratio change $\geq$ 0.2 and body column volume change < 0.2, isotropic expansion is defined by normalized aspect ratio change < 0.2 and body column volume change $\geq$ 0.2, and anisotropic expansion is defined by normalized aspect ratio change and body column volume change $\geq$ 0.2. If none of these criteria are met, the morphodynamics at that given time point is labeled 'no elongation' to indicate that the animal either decreased or did not substantially increase in aspect ratio and/or volume.

To visualize contraction dynamics in kymographs, the measurements for body column diameter along the oral-aboral axis (excluding the caps at the extremities) were plotted over time, where the color represents the diameter and the y-location reflects the location along the oral-aboral axis. Here the data was stretched to fit to the actual body column length (including the correction for the extremities). The morphodynamics for 5-second resolution data (Figure 2F) were calculated using a cut-off period of 83 minutes, in order to see the dynamics in a narrower but more densely sampled time window.

Optical coherence microscopy and data processing

Optical Coherence Microscopy (OCM) has emerged as a promising modality for three-dimensional morphological imaging of small, behaving animals because of its high volumetric speed, label-free contrast and non-phototoxicity.[80] Here we developed a bespoke OCM platform optimized for in-vivo imaging and biometry of non-anesthetized *Nematostella*. Because light scattering, absorption, and shadowing artefacts, especially at the larval stage, did not permit whole animal imaging, we engineered a tailored, dual-view spectral-domain Optical Coherence Microscopy (DV-OCM) system that permitted quantitative 3D mapping at a high and near-isotropic spatial resolution (2.3/2.0 μm laterally/axially). The dual-view geometry was essential to obtain accurate and reliable tissue/cavity volume measurements across the whole animal. Figure S2C shows the schematic diagram of the DV-OCM system, which incorporates two identical illumination/detection arms that are symmetric with respect to the intermediate plane between the two objective lenses. The collimated illumination was first focused by a scanning lens (f = 50 mm, Plossl lens build from two f = 100 mm achromats, EdmundOptics, 47-317). Then a knife-edge right angle prism mirror (Thorlabs, MRAK25-P01) was used to equally split the probe beams into the two scanning arms. Each optical arm contained a tube lens (Thorlabs, TTL200-S8) and an objective lens (Nikon, Plan Fluor 4x, NA 0.13) both of which were carefully co-aligned to focus the light on the same spot on the sample plane. The laser source for OCM imaging was a supercontinuum laser (YSL Supercontinuum Source SC-PRO 7), of which the spectrum was custom-filtered to cover the band 760-920nm (center wavelength 832 nm), and fed into a 20/80 fiber-coupler based interferometer. A custom-built k-wave spectrometer[81] recorded the interference signals on a 2048 pixels, 28 kHz line camera (AViiVA SM2 CL, e2v, Cedex, France). The measured lateral and axial resolution in tissue (n=1.35) was ~2.3 and 2.0μm, respectively. A profile of depth scan (A-line) was reconstructed from the interference spectral signal following a regular OCT postprocessing procedure including dispersion compensation, background subtraction, spectrum reshaping and inverse fast Fourier transformation[82] and was saved as individual TIFF files using a custom Matlab (v2019b) script. Each cross-sectional image (B-scan) contained 512 A-lines and was split into two images obtained from the different views. In order to record a single 3D image stack, 256 B-scans were performed which took ~ 4.7s in total. The image acquisition was controlled by a custom-written Labview program which synchronized the galvo scanners (Cambridge, VM500+) and read-out the spectrometer via an FPGA card (NI, NI PCIe-7841R).

For imaging, live non-anesthetized larvae and polyps were sandwiched between two coverslips with spacers and mounted on a stage with manual x,y,z movement.

The raw OCM images were post-processed using FIJI[60] (v1.53c) by median filtering with 2 pixel width to remove speckle noise followed by a re-scale operation to correct for the difference between the axial and lateral voxel dimensions. Alignment was performed using Fijiyama (automatic registration, block matching, default settings).[65] The two views were combined into one volume and then segmented into tissue and cavity using the trainable WEKA segmentation FIJI plugin[66] and ilastik,[83] followed by manual correction and clean-up. Tissue volume and cavity were calculated from the segmented masks using the IntrinsicVolumes3D function from the MorpholibJ package.[62] 3D views were created with VolumeViewer (2.01) in FIJI (https://imagej.nih.gov/ij/plugins/volume-viewer.html).

Pressure measurements

The 900A micropressure system (World Precision Instruments, SYS-900A) was used to perform direct measurements of body cavity pressure according to the manufacturer's instructions and adapted from previous work.[32,33] A pre-pulled micropipette of tip diameter 1μm (WPI, TIP1TW1) was filled with 1M KCl solution using a MicroFil flexible needle (WPI, MF34G-5), placed in a microelectrode holder half-cell (WPI, MEH6SF) and connected to a pressure source regulated by the 900A system (WPI, 900APP). Prior to making a pressure measurement, each new microelectrode was calibrated using a calibration chamber (WPI, CAL900A) filled with 0.1M KCl solution. The microelectrode and a reference electrode (WPI, DRIREF-2) were then mounted onto the micromanipulator (Narishige MO-202D) within an inverted Zeiss Axio Observer microscope.

To prepare the animals for pressure measurement, polyps were first placed onto 6-cm Petri dishes in ASW with or without pharmacological inhibitors, and allowed to adhere to the bottom surface. The dish was mounted on the microscope with the reference electrode immersed in the medium, and the microelectrode was then lowered into the sample dish and inserted into the cavity of the animal by piercing through the muscular body wall. The microelectrode was then maintained in place to record the pressure reading for up to 8-10 minutes, ensuring that the tip was visible. A time-lapse video of the animal was recorded simultaneously with the measurement of pressure to capture contractions. Data that showed a very rapid increase or decrease in pressure within 10s of probe insertion were discarded, as these indicate blockage of the micropipette during insertion or substantial leakage through rupture, respectively. The change in cavity pressure was then plotted as a function of time, overlaid with the time-lapse video to identify the period of muscle contractions.

Pharmacological treatments

To test the short-term effect of muscle anesthetics on body contractions, animals were directly incubated in a 384-well plate with one of the following drugs: 1 mM linalool[35] (Sigma, L2602) with 0.03% DMSO, 400 μM menthol[30,34] (Sigma, M2772) with 0.1% DMSO, 3.5% or 0.5% $MgCl_2$, or 0.5 mM rocuronium bromide[84] with 0.2% DMSO (Sigma, R5155). Animals were imaged at 5-second or 30-second interval for up to one hour using the Acquifer microscope and analyzed using the described image analysis pipeline.

To test the effect of muscle anesthetics on development, animals were incubated in 1 mM linalool[35] (Sigma, L2602) with 0.03% DMSO, 400 μM menthol[30,34] (Sigma, M2772) with 0.1% DMSO, 0.5% $MgCl_2$, or 0.5 mM rocuronium bromide[84] with 0.2% DMSO (Sigma, R5155) in glass dishes for three days. As a control, animals were incubated in either 12 ppt ASW or 12 ppt ASW with 0.2% DMSO. For the *BMP2/4* KD experiment in combination with inhibition of muscle contraction, we injected fertilized eggs with *BMP2/4* shRNA (550 ng/μl). Animals were either fixed after 2 days (t_0) or incubated in 0.1% DMSO (control), 400 μM menthol with 0.1% DMSO, or 1 mM linalool with 0.03% DMSO for 4 days. All dishes were sealed with parafilm without refreshing the drug solutions. Fixed samples were stained with phalloidin Alexa Fluor 546 (Thermo Fisher, A22283, 1:100), and mounted in glycerol on microscope slides. All samples were imaged using a Zeiss LSM 780 NLO or LSM 880 confocal inverted microscope with Plan-Apochromat 20x/0.8 objective. Body length was measured by drawing a segmented line from the oral to the aboral pole in the midplane of the animal. Area of body cavity and internal tissues in the mid-plane section was measured in FIJI by manual segmentation.

To test the role of cell proliferation during development, budded larvae were treated with 5 mM hydroxyurea (HU) (Sigma, h8627) in ASW while controls were incubated in 12 ppt ASW. For high-throughput imaging, animals were transferred in a 384-well plate containing 25 μl 5 mM HU or 25 μl 12 ppt ASW for controls. Animals were imaged at 5-minute time resolution for up to 80 hours at 27 °C using the Acquifer microscope with the brightfield channel. For immunostaining, animals were kept in glass dishes at 27 °C and were fixed after 3 and 24 hours of incubation.

Fixation and immunostaining

Animals were anesthetized in 7% $MgCl_2$ prior to fixation. Fixation was performed for 1 hour at room temperature either with 4% paraformaldehyde (EMS, E15710) in PBS with 0.1% Tween (PTw 0.1%, Sigma, P1379) for phosphorylated histone 3 antibody staining[85] (pH3, Sigma # 05-806, 1:100), or with Lavdovsky's fixative following the described protocol[42] (3.7% formaldehyde, 50% ethanol, 4% acetic acid) for Cadherin3 antibody detection (gift from Technau lab,[42] 1:500). Animals were permeabilized in 10% DMSO (Thermo Fisher, 85190) in PBS for 20 minutes and washed with PBS with 0.2% Triton (Sigma, T8787) (PTx 0.2%), followed by 1-hour incubation in blocking buffer containing PTx 0.1%, 0.1% DMSO, 1% BSA (Sigma, A2153), and 5% Goat serum (Sigma, G9023). Samples were incubated with the primary antibody in blocking solution overnight at 4 °C. After washing with PTw 0.1%, animals were incubated with the secondary antibody goat-anti-mouse Alexa-488 (Thermo Fisher, A-11001, 1:500) or donkey-anti-mouse Alexa-488 (Thermo Fisher A21202, 1:500) in PTx 0.1% overnight at 4 °C. For (additional) staining for F-actin and nuclei, phalloidin Alexa Fluor 546 (Thermo Fisher, A22283, 1:100) and Hoechst 34580 (Sigma, 63493, 1:1000) were used, in PTx 0.1% overnight at 4 °C. Finally, animals were washed in PTw 0.1% and cleared in 80% glycerol (Merck).

Confocal imaging

Samples were imaged using a Zeiss LSM 780 confocal inverted microscope with Plan-Apochromat 20x/0.8 objective, or using a Zeiss LSM 880 point scanning confocal microscope controlled with the Zeiss Zen 2.3 (black edition) software, with Plan-Apochromat 20x/0.8 air objective. To image epidermal cells, we used a Plan-Apochromat 40x/1.4 Oil DIC objective, AiryFast mode and tile scans, at 0.5 μm z-resolution. Depending on the staining, we used laser lines diode 405 nm, argon multi-line 458/488/514 nm and/or HeNe 561 nm.

Quantification of cellular properties

The number of pH3-positive mitotic cells was counted manually in FIJI and normalized to the imaged tissue volume. Epidermal thickness was measured manually in images of the mid-plane of the animal at multiple locations along the body axis using FIJI. The measurement was taken in the mid-body region between 30% and 70% of the total length of the oral-aboral axis. Quantifications of the cell apical surface area were based on the images taken with the 40x magnification objective. To correct for the typical uneven surface of the animals and the body column deflation upon addition of glycerol, the Minimum cost Z surface projection FIJI plugin (https://imagej.net/plugins/minimum-cost-z-surface-projection)[64] was used to obtain separate, flattened layers for the ectoderm tissue and the underlying muscular tissue (shown in Figures 5A–5C, 6C, and S3J). Next, one or more flattened slices showing cell boundaries were selected and used as input for detection of cells by Cellpose[43] (v1.0, 2D mode, model-type cytoplasm). The mask produced by Cellpose was converted to a label image and was manually corrected. For phalloidin staining in polyps, correctly segmented cells were manually selected. Cell area was obtained using the MorphoLibJ package.[62] Muscle fiber orientation was measured using the Directionality plugin in FIJI (https://github.com/fiji/Directionality).

shRNA design and synthesis

shRNAs were designed based on previous work[26] and using the siRNA Wizard from Invivogen (available at https://www.invivogen.com/sirnawizard/design_advanced.php). Primers were synthesized by Sigma and IDT.

Primers were annealed at 98 °C for 5 min in the PCR machine or heat block and allowed to cool down to room temperature. shRNA was synthesized using the T7 MegaShortScript kit (Invitrogen, AM1354) with an incubation time of 6 hours, followed by a purification step using magnetic SPRISelect beads (Beckman Coulter B23319) in the presence of 46% isopropanol.[86] Samples were incubated

for 15 minutes at room temperature, and were then placed in magnetic stands for 5 minutes, until the solution appeared clear. The samples were washed twice using 80% freshly prepared ethanol, after which they were shortly dried and resuspended in RNase free water. The solution was aliquoted and stored at -80 °C.

Microinjection of shRNAs

Unfertilized eggs were dejellied in 4% cysteine solution (Sigma, 168149) in ASW for 9 minutes and washed with ASW. Eggs were then fertilized and injected with shRNA targeting GFP, Tbx20 or BMP (500–1500 ng/μl), combined with Texas Red-labelled Dextran (ThermoFisher, D3328) using a Femtojet Express (Eppendorf). Injected eggs were kept at room temperature and transferred to 27 °C the following day.

Quantification of *Tbx20* expression after shRNA knockdown

Animals were injected with either *Tbx20* or GFP shRNA. At 4 DPF, pools of 40 larvae were collected in TRI reagent (Zymo Research) for total RNA isolation using a phenol-chloroform based extraction. Isolated RNA was treated with DNase I (NEB) and the concentration measured using the Qubit RNA BR kit (Thermo Fisher Scientific). For cDNA synthesis (ImPromII RT kit, Promega), 50 ng total RNA of each sample was used. A cDNA standard curve was generated by using 200, 100, 50, 25, 12.5, 6.3 and 0 ng cDNA. Quantification of expression was done by qPCR using the SYBR Green PCR Master Mix kit (Thermo Fisher Scientific) according the manufacturer's instructions. For normalization gene selection, expression levels of the housekeeping genes *Actin*, *Gapdh* and *Atp5f1b* during development were used as input for RefFinder software.[87] *Atp5f1b* showed the most stable expression during development and was selected for this study. Sequences of qPCR primers used were:

Tbx20.1F: 5'-GGACCACACAGCGTCAGTAA-3';
Tbx20.1R: 5'-AAGGTTGTCGAGGGGAAAGT-3';
Tbx20.2F: 5'-CGCTGAGATGTGTCTGGAAG-3';
Tbx20.2R: 5'-CGCCTCCCTGACTTTGTTAT-3'
Atp5f1b-F: 5'-CGTTATTGGAGAGCCTATTGATG-3';
Atp5f1b-R: 5'-CCTGCTCTGTGCTCATTTC-3'.

CRISPR/Cas9

Single guide RNAs (sgRNAs) were designed using the online web interface http://chopchop.cbu.uib.no.[67] To perform an F0 phenotypic analysis of the double KO of Tbx20 paralogs, a total of two sgRNAs targeting both genes were used. The two gRNAs were commercially synthesized (Sigma aldrich). The sequence targets were: sgRNA-1: ACGTTGCGGATCTCCGTGAGTGG and sgRNA-2: CCCTGACTCACCGTTCACGGGGG. These sequences are identical in both Tbx20 paralogs. Recombinant Cas9 protein (900 ng μl^{-1}; PNA Bio, #CP01-20) was co-injected with both sgRNAs (20μM each) into unfertilized *Nematostella* oocytes. Injected oocytes were then fertilized and raised at room temperature for imaging and sequencing.

Genotyping of *Tbx20* F0 animals

F0 adults were left undisturbed until they were fully relaxed and 7% $MgCl_2$ was carefully added to the dish to immobilize them. After taking images using a Leica stereoscope, a small piece of tentacle (~2-3 mm) was collected for genotyping. Genomic DNA isolation was performed by incubation of the tissue for 2 hours at 65°C in QuickExtract DNA Extraction Solution (Lucigen) and subsequent heat inactivation. A standard PCR using Phusion polymerase (Thermo Fisher Scientific) was used to amplify fragments for Sanger sequencing of the Tbx20-1 and Tbx20-2 genes. The following primers were used:

Tbx20.1F: 5'-TTGGCATTTCATTTTTAAAGCA-3';
Tbx20.1R: 5'-CCTCTTGTATTCACTGATGCAAAT-3';
Tbx20.2F: 5'-TGAAGTTTCTTGTGTGATTAATTTTGC-3';
Tbx20.2R: 5'-TCATCAATAGACGAGTTCAATTTTAGC-3'.

Photoconversion of Kaede

mRNA was synthesized using the HiScribe™ T7 ARCA mRNA Kit (with tailing) (NEB, E2060S) and a PCR product amplified from the Kaede-NLS plasmid (addgene, 57319) (primers are shown in key resources table). Following mRNA purification with magnetic SPRISelect beads (Beckman Coulter B23319), fertilized eggs were co-injected with a solution mix containing Kaede-NLS mRNA (200 ng/μl), shRNA targeting BMP (430 ng/μl) or Tbx20 (560 ng/μl), and FITC (ThermoFisher, 46425). Control embryos were only injected with Kaede-NLS mRNA and FITC. Photoconversion of Kaede[69] was performed on anesthetized larvae on a Zeiss LSM 780 microscope with Plan-Apochromat 20x/0.8 objective, using the 'bleaching' and 'regions' option, and using the 405 laser at 0.6% laser power, with 80 iterations. Imaging of developed animals after photoconversion was performed on a Zeiss LSM 780 or 880, with Plan-Apochromat 20x/0.8 objective.

Biophysical manipulation

Glass capillaries (TW100F-4, World Precision Instruments) were pulled using a micropipette puller to obtain approximately 10μm diameter tubes. To create openings across the tube length, pulled capillaries were mounted in an imaging slide with double-side tape, and laser-cut holes were created using the 355 nm laser of the Olympus FV1200 microscope. During the piercing of the larvae, open and closed capillaries were handled with a joystick for micro-injection (MO-202U, Narishige-group). For open capillaries, the pressure was equalized using the compensation pressure function of the Eppendorf electronic microinjector, the FemtoJet®.

Biophysical model

Geometry

For a thin cylindrical shell with length $\ell(t)$, radius $r(t)$, wall thickness $h(t)$, the changes of cylindrical shell thickness are neglectable, i.e., $h(t) \approx h$. The conservation of the cavity volume V_C is given as

$$\frac{dV_C}{dt} = \frac{d}{dt}\left(r^2 \ell\right) = Q_{\text{water}}, \qquad \text{(Equation 1)}$$

where the water flux is further assumed as $Q_{\text{water}} \approx 0$, and thus the cavity volume is constant during the shape evolution of the larva to polyp. This constant cavity volume condition indicates that when the length of the shell keeps increasing, its radius is decreasing. To understand the basic conceptual model underlying mechanical morphogenesis driven by the hydraulic stresses due to fluid pressure, we limit ourselves to the case of small strains, so that the axial and azimuthal strains can be written as

$$\varepsilon_z = \varepsilon_z^{\text{a}} + \varepsilon_z^{\text{p}} = (\ell - \ell_0)/\ell_0 > 0 \text{ and } \varepsilon_\theta = \varepsilon_\theta^{\text{a}} + \varepsilon_\theta^{\text{p}} = (r - r_0)/r_0 < 0. \qquad \text{(Equation 2)}$$

Hereafter, the superscript 'a' and 'p' represent the active and passive elements, respectively. A geometrically nonlinear model that might be written in terms of the logarithmic strain measures and more complex constitutive models, but will only change our results quantitatively.

Mechanical equilibrium and active morphogenesis of body wall

All asymmetries in the relative stiffnesses in the principal directions can be ascribed to the difference in the densities of the azimuthal muscle fibers versus the axial muscle fibers. Since the body wall is capable of irreversible deformations over developmental times, we assume that it can be modeled as an orthotropic active elastic visco-plastic material, with E_z^{p} being the passive axial elastic modulus and E_θ^{p} being the passive azimuthal elastic modulus of the wall, and η the effective viscosity of the wall. For simplicity, we assume that the active moduli of the muscles in the axial and azimuthal directions are E_z^{a} and E_θ^{a}, respectively, so that the stresses of the axial and azimuthal muscular springs can be modeled as $\sigma_z^{\text{a}} = E_z^{\text{a}}\varepsilon_z^{\text{a}}$ and $\sigma_\theta^{\text{a}} = E_\theta^{\text{a}}\varepsilon_\theta^{\text{a}}$.[88] The active contractile element can be activated by the biological signals such as calcium ion and electrical stimulation, and external mechanical stimulation.[88] When the action potential exceeds a threshold, the contractile element is activated and can generate active contraction σ^{A} which compresses the passive element. Considering a linear elastic orthotropic shell with two main directions in x_1 and x_2, the general constitutive relation is $\sigma_{11} = E_1\varepsilon_{11}/(1-\nu_{12}\nu_{21}) + \nu_{21}E_2\varepsilon_{22}/(1-\nu_{12}\nu_{21})$ and $\sigma_{22} = E_2\varepsilon_{22}/(1-\nu_{12}\nu_{21}) + \nu_{12}E_1\varepsilon_{11}/(1-\nu_{12}\nu_{21})$ with $\nu_{21}E_2 = \nu_{12}E_1$. For simplicity, we assume the Poisson's ratios in both directions vanishing, i.e., $\nu_{12} = \nu_{21} = 0$. This assumption implies the tissue volume $V_T = 2\pi rhl$ is not constant.

The shell is subject to a combination of a static basal muscle tonus and a dynamic muscular contractile stress which leads to a hydraulic pressure that we write as $P(t) = p_T + p_0\cos(2\pi\omega t)$. The equations of axial and azimuthal mechanical equilibrium read

$$\sigma_z = \sigma_z^{\text{a}} = \sigma_z^{\text{p}} + \sigma_z^{\text{A}} = \frac{Pr}{2h} \text{ and } \sigma_\theta = \sigma_\theta^{\text{a}} = \sigma_\theta^{\text{p}} + \sigma_\theta^{\text{A}} = \frac{Pr}{h}. \qquad \text{(Equation 3)}$$

Combining Equations 2 and 3, we see that the shell is always stretched along the axial direction, indicating that the axial contractile element is not activated ($\sigma_z^{\text{A}} = 0$). Due to the dynamic changes of hydraulic pressure, the shell experiences several axial loading and unloading cycles during which the axial passive element accumulates plastic and viscous axial strains, as shown in Figure 4B. However, in azimuthal direction, the total strain ε_θ remains negative, indicating that the azimuthal contractile element is activated ($\sigma_\theta^{\text{A}} > 0$), and the azimuthal passive element is always under compression. Considering this scenario where the passive element is axially stretched and azimuthally compressed, we adopt a minimal model corresponding to perfect elastic viscoplasticity for the passive element, and write the corresponding constitutive relation as

$$\sigma_z^{\text{p}} = \begin{cases} E_z^{\text{p}}\varepsilon_z^{\text{p}} & \left(\sigma_z^{\text{p}} < \sigma^y\right) \\ \sigma^y + \eta\dot{\varepsilon}_z^{\text{p}} & \left(\sigma_z^{\text{p}} \geq \sigma^y\right) \end{cases}, \text{ and } \sigma_\theta^{\text{p}} = E_\theta^{\text{p}}\varepsilon_\theta^{\text{p}}, \qquad \text{(Equation 4)}$$

where the yield stress is assumed to satisfy the inequality $p_T < 2\sigma^y h/r_0 < p_T + p_0$ ensuring the basal (static) pressure does not lead to irreversible axial yielding but the dynamic pressure can and does lead to yielding cycles. Therefore, the yield stress can be assumed as

$$\sigma^y = \frac{(p_T + \alpha p_0)r_0}{2h} \text{ with } 0 < \alpha < 1. \qquad \text{(Equation 5)}$$

Figure 4B shows the stress-strain curves during the loading-unloading cycles driven by the hydraulic pressure oscillations. At the beginning, the axial stress $\sigma_z = \sigma_z^{\text{p}}$ increases with pressure during the first oscillation period (inclined red line), and the system behaves elastically until the axial strain reaches $\varepsilon_z = \varepsilon_{c0} = \sigma^y/E_z^{\text{a}} + \sigma^y/E_z^{\text{p}}$. As the pressure continues to increase, the shell yields axially

and starts to flow following the relation $\sigma_z = \sigma_z^p = \sigma^y + \eta\dot{\varepsilon}_z^p$, beginning to accumulate irreversible axial plastic strain (horizontal red line). When the oscillating pressure starts to decrease, the axial stress $\sigma_z = P(t)r(t)/(2h) = P(t)/(2h\sqrt{1+\varepsilon_z})$ also decreases for a while while the axial strain continues to increase (horizontal blue line). This viscoplastic response lasts until the pressure-induced axial stress becomes lower than the yield stress, and corresponds to the case when the strain is $\varepsilon_z = \varepsilon_{c1}$. Then the system unloads elastically. The next loading cycle (inclined blue and red lines) follows a similar pattern as the pressure-induced axial stress reaches the yield stress again, leading to irreversible viscoplastic flow, followed by elastic unloading. As these cycles are repeated, the maximum pressure-induced axial stress keeps decreasing (because the radius of the shell decreases) until eventually the stress equals to the yield stress, corresponding to a critical radius r_{cr} satisfying $(p_T + p_0)r_{cr}/(2h) = \sigma^y$ and the critical axial strain $\varepsilon_{cr} = (r_0/r_{cr})^2 - 1$. After this critical point is reached, the system responds to the pressure oscillations via periodic and reversible elastic deformations about a new equilibrium length and raidus.

Combining Equations 1, 2, 3, and 4, we can solve for the variations of the length and radius of the polyp as a function of time (Figure 4C), with the initial conditions $\ell(0) = \ell_0$ and $r(0) = r_0$, and typical parameter values:[36] $E_z^a = E_z^p = 500\text{kPa}, p_T = 5\text{Pa}, p_0 = 1\text{Pa}, \alpha = 0.5$, $\eta = 10\text{Pa}\cdot\text{s}, r_0 = 100\mu\text{m}, \ell_0 = 300\mu\text{m}, h_0 = 10\mu\text{m}$. The characteristic time is $t^* = \eta/E_z^p$ and the characteristic frequency is $\omega^* = 1/t^*$. To understand the results qualitatively, we show below the results of multiple loading cycles as the stress varies dynamically – the shell yields periodically in the longitudinal direction (see also Video S5) and eventually reaches a new equilibrium length and radius (Figure 4C).

At steady state, the strain rates vanish, and the body wall tissue volume remains conserved which implies that $rh\ell = const$. In *Tbx20* KD animals, we expect that the elastic stiffness resulting from the disorganized parietal and circular muscles becomes negligible, so that the axial and azimuthal stiffnesses are similar, i.e, $E_z^p \approx E_\theta^p$. With these assumptions, Equations 3 and 4 yield $\varepsilon_\theta = \varepsilon_z$, i.e. *Tbx20* KD larvae will isotropically inflate via fluid uptake to form a spherical polyp morphology. In contrast, *BMP2/4* KD animals only maintain the circular muscles, implying that effective stiffness in the azimuthal direction is greater than the stiffness in axial direction, $E_\theta \gg E_z$. Then the equilibrium relationship (Equation 3) simplifies to: $E_\theta\varepsilon_\theta = 2E_z\varepsilon_z$ and furthermore the cavity volume is conserved, i.e. $r^2\ell = const$. These simple relations explain the origin of a thin and elongated morphology with a conserved cavity volume ($2\dot{r}\ell + r\dot{\ell} \approx 0$) and large aspect ratio ($\ell/2r \gg 1$) while having negligible changes in body wall thickness $h(t) \approx h_0$. Finally, wild type animals inflate their cavity through fluid uptake ($2\dot{r}\ell + r\dot{\ell} > 0$), while the body wall tissue volume does not change $rh\ell = const$. As a consequence, a similar situation to the *BMP2/4* KD animals is obtained, i.e. the aspect ratio $\ell/2r$ can be larger than unity if the axial stiffness is lower than the azimuthal stiffness, i.e. $E_z/E_\theta < 1$ since then the body geometry will imply that the axial strain will be larger than the azimuthal strain, i.e. $\varepsilon_z/\varepsilon_\theta > 1$.

Physical balloon experiments

For the physical simulacrum experiments, we used latex balloons (12" Balloons, red, Celebrate It™, Item No: 10108443), elastic braided bands (1/4" Braided Elastic Hank, Loops & Threads™, Item No: 10187887), inextensible electrical tapes (3/4", pressure sensitive vinyl tape, red, Gardner Bender) and stretchable adhesive (Loctite vinyl fabric & plastic flexible adhesive, Item No: 1360694). To mimic the various *Nematostella* phenotypes, our initial starting point is identical, the uninflated latex balloon (Figure S5A), which when inflated using compressed air, expands isotropically with aspect ratios 1, serving as a control for the following mimic experiments (Figure S57B). To obtain the *Tbx20* KD phenotype, we first inflate the balloon such that it extends basally (volume $\sim V_0$). We then stick small pieces of extensible tapes in randomized orientation (here, tapes serve as proxy for muscles on the elastic wall of the balloons), following further inflation (volume $\sim V_f$), thereby obtaining close to spherical shapes (aspect ratios in the range of $\ell/d \sim 1.1$-1.3 and volume change ratios in the range of $V_f/V_0 \sim 2.5$-5.5) (Figure S5C). Wildtype mimics are obtained using two methods: (I) the balloon is inflated basally, followed by attaching thin elastic bands azimuthally with the stretchable adhesive. The elastic bands make the azimuthal stiffness of the balloon larger than its axial stiffness. When this balloon is inflated, it elongates longitudinally, mimicking the shape changes in wild type polyps with aspect ratios $\ell/d \sim 2$ and volume changes $V_f/V_0 \sim 2$-4 (Figure S5D). The second method (II) to obtain wildtype mimics employs a slightly different approach wherein the balloon is inflated more at the beginning, sealed, and then stretched longitudinally while attaching inextensible tapes helically. This determines the volume change at the beginning and is followed by remodeling of the balloon wall to yield slender shapes ($\ell/d \sim 4.2$-5 and $V_f/V_0 \sim 2.5$-4, here V_f/V_0 is obtained by comparing the inflated balloon stage before remodeling with the basally inflated stage) (Figure S5E). To obtain the *BMP2/4* KD mimic, we needed to obtain much larger aspect ratios, and it is known from experiments that the cavity volume remains constant during the transformation of polyps. We first inflated the balloons to a basally distended shape and sealed the opening of the balloon. The inflated balloon mimicking the larval stage was then stretched axially and taped with inextensible pressure sensitive vinyl tapes (electric tapes) to constrain the azimuthal direction while elongating in the axial direction. This led to high aspect ratios $\ell/d \sim 7.5$ while keeping the cavity volume constant ($V_f/V_0 = 1$) (Figure S5F). Using the simple toolbox of balloons, elastic bands, electrical tapes and adhesives, we are able to recapture the steady state phenotypes and the phase space of *Nematostella* animals.

QUANTIFICATION AND STATISTICAL ANALYSIS

Data analysis and generation of plots was performed in RStudio version 1.1.442,[70,71] making use of the tidyverse,[72] ggplot2,[73] ggpubr,[74] gtable,[75] and ggrastr[76] packages, and Prism 8. Wilcoxon rank sum tests were used for significance testing, unless mentioned otherwise. The forecast package[77,78] was used to remove outliers in time sequence data.